

Misaligned Wind-Waves Behind Atmospheric Cold Fronts

Cesar Sauvage¹, Hyodae Seo¹, Benajmin W. Barr², James B Edson¹, and Carol Anne Clayson³

¹Woods Hole Oceanographic Institution

²woods hole oceanographic institution

³WHOI

April 11, 2024

Abstract

Atmospheric fronts embedded in extratropical cyclones are high-impact weather phenomena, contributing significantly to mid-latitude winter precipitation. The three vital characteristics of the atmospheric fronts, high wind speeds, abrupt change in wind direction, and rapid translation, force the induced surface waves to be misaligned with winds exclusively behind the cold fronts. The effects of the misaligned waves on air-sea fluxes remain undocumented. Using the multi-year in situ near-surface observations and direct covariance flux measurements from the Pioneer Array off the coast of New England, we find that the majority of the passing cold fronts generate misaligned waves behind the cold front. Once generated, the waves remain misaligned, on average, for about 8 hours. The fully-coupled model simulations indicate that the misaligned waves significantly increase wave roughness length (300%), drag coefficient (30%), and momentum flux (20%). The increased surface drag reduces the wind speeds in the surface layer. The upward turbulent heat flux is weakly decreased by the misaligned waves because of the compensating effect between the decrease in temperature and humidity scaling parameters and the increase in friction velocity. The misaligned wave effect is not accurately represented in a commonly used wave-based bulk flux algorithm. Yet, the suggested modification to the current formulation improves the overall accuracy of parameterized momentum flux estimates. The results imply that better representing a directional wind-wave coupling in the bulk formula of the numerical models may help improve the air-sea interaction simulations under the passing atmospheric fronts in the midlatitudes.

Misaligned Wind-Waves Behind Atmospheric Cold Fronts

César Sauvage¹, Hyodae Seo¹, Benjamin W. Barr¹, James B. Edson¹, and Carol Anne Clayson¹.

¹Woods Hole Oceanographic Institution, Woods Hole, Massachusetts, USA

Key Points:

- Passing atmospheric cold fronts generate a large area of growing wind-waves that are misaligned with local wind.
- The misaligned waves increase the roughness length, drag and enthalpy exchange coefficients, and wind stress.
- Representation of the misaligned wave effect in the bulk formula improves the momentum flux estimates.

Corresponding author: César Sauvage, csauvage@whoi.edu

Abstract

13 Atmospheric fronts embedded in extratropical cyclones are high-impact weather phenom-
14 ena, contributing significantly to midlatitude winter precipitation. The three vital char-
15 acteristics of the atmospheric fronts, high wind speeds, abrupt change in wind direction,
16 and rapid translation, force the induced surface waves to be misaligned with winds ex-
17 clusively behind the cold fronts. The effects of the misaligned waves on air-sea fluxes re-
18 main undocumented. Using the multi-year in situ near-surface observations and direct
19 covariance flux measurements from the Pioneer Array off the coast of New England, we
20 find that the majority of the passing cold fronts generate misaligned waves behind the
21 cold front. Once generated, the waves remain misaligned, on average, for about 8 hours.
22 The fully-coupled model simulations indicate that the misaligned waves significantly in-
23 crease the roughness length (300%), drag coefficient (30%), and momentum flux (20%).
24 The increased surface drag reduces the wind speeds in the surface layer. The upward tur-
25 bulent heat flux is weakly decreased by the misaligned waves because of the compensat-
26 ing effect between the decrease in temperature and humidity scaling parameters and the
27 increase in friction velocity. The misaligned wave effect is not accurately represented in
28 a commonly used wave-based bulk flux algorithm. Yet, the suggested modification to the
29 current formulation improves the overall accuracy of parameterized momentum flux es-
30 timates. The results imply that better representing a directional wind-wave coupling in
31 the bulk formula of the numerical models may help improve the air-sea interaction sim-
32 ulations under the passing atmospheric fronts in the midlatitudes.
33

Plain Language Summary

34 Atmospheric fronts are recurrent weather phenomena in midlatitudes, significantly
35 contributing to winter precipitation. They are characterized by high wind speeds, abrupt
36 change in wind direction, and rapid translation. Their passage over the ocean lead to
37 the generation of strongly misaligned waves, particularly behind the cold fronts. The ef-
38 fects of these misaligned waves on air-sea fluxes remain undocumented. Using the long
39 term surface observations from the Pioneer Array off the coast of New England, we find
40 that the majority of the passing atmospheric fronts generate misaligned waves behind
41 the cold front which can remain misaligned, on average, for about 8 hours. The use of
42 coupled numerical experiments indicate that the misaligned waves significantly increase
43 the ocean roughness length and momentum flux, which reduce the surface wind speeds.
44

45 The misaligned wave effect is not accurately represented in a commonly used wave based
46 air-sea flux algorithm. Yet, the suggested modification to the current formulation im-
47 proves the overall accuracy of parameterized momentum flux estimates. The results im-
48 ply that better representing a directional wind-wave coupling in numerical models may
49 help improve the air-sea interaction simulations under the passing atmospheric fronts
50 in the midlatitudes.

51 **1 Introduction**

52 Air-sea momentum, heat, and moisture exchanges are mediated by interactions be-
53 tween near-surface atmospheric turbulence and the ocean surface wave field. Wave fields
54 are complex and may include contributions from a wide range of frequencies and direc-
55 tions, including strongly coupled short wind-waves with wavelengths of $O(0.1-10\text{ m})$ and
56 frequencies higher than twice the spectral peak (Phillips, 1966; Makin et al., 1995; Kukulka
57 & Hara, 2005), developing to mature locally generated wind-waves and remotely gen-
58 erated long-period swell. In many current modern sea state-dependent (or wave-based)
59 bulk flux algorithms, the surface waves that determine the surface drag are often assumed
60 to be in the direction of winds. However, there are many wind and wave regimes where
61 this assumption is not valid and where using it can yield notable deficiencies in the pa-
62 rameterized momentum flux. Swell waves under the low-wind condition (Grachev & Fairall,
63 2001; G. Chen et al., 2002; Hanley & Belcher, 2008; Hanley et al., 2010; Sullivan et al.,
64 2008) or the mixed seas under the trade wind (Sauvage et al., 2023) or tropical cyclones
65 (S. S. Chen et al., 2013; Reichl et al., 2014; S. S. Chen & Curcic, 2016; Hsu et al., 2019;
66 X. Chen et al., 2020) are well-known examples in the lower-latitudes. Existing studies
67 suggest a complex relationship between wind-wave misalignment and surface stress, which
68 may be regime-dependent (e.g., high winds in tropical cyclones vs. lower winds in mid-
69 latitudes). For instance, Zhou et al. (2022) found that misalignment between local winds
70 and tropical cyclone-generated swell reduced the drag coefficient in high winds, suggest-
71 ing quadrant-specific variations in drag due to storm-scale misalignment patterns. On
72 the other hand, Porchetta et al. (2019) examined in situ observations from the North Sea
73 and the U.S. New England coast and found that wind-wave misalignment increases the
74 surface drag, with additional influence by wave age.

75 In the midlatitudes, the atmospheric fronts are embedded in the extratropical cy-
76 clones and significantly modulate the day-to-day weather variability. They feature elon-

77 gated along-frontal scales of 1000s km comparable to the lateral extent of the extratrop-
78 ical cyclones, but much shorter cross-frontal scales of 10-100 km (Figure 1, Bjerknes &
79 Solberg, 1922). Figure 1a shows a typical extratropical cyclone we will examine in this
80 study. Traveling rapidly eastward at ≈ 10 m/s, the atmospheric fronts accompany gale-
81 force near-surface winds (15-30 m/s), which also abruptly shift in direction from the southerly
82 in the warm sector to the northwesterly in the cold sector. Although atmospheric fronts
83 typically occur 10-30% in the wintertime North Atlantic (Hewson, 1998; Berry et al., 2011;
84 Parfitt et al., 2017; Reeder et al., 2021), they are known to contribute to up to 90% of
85 the precipitation (Catto & Pfahl, 2013; Soster & Parfitt, 2022), often in an extreme form
86 (Catto & Pfahl, 2013) and, hence, they are one of the most important high-impact weather
87 phenomena in the midlatitudes. Interactions between the cold airmass of the fronts and
88 the warmer ocean (and ocean fronts) via air-sea turbulent heat fluxes influence the in-
89 tensity of these events (Parfitt et al., 2016; Seo et al., 2023). The atmospheric cold fronts
90 are also known to force significant surges and complex wave reactions that severely im-
91 pact coastal and estuary circulations and wetland evolutions (Kim et al., 2020; Cao et
92 al., 2020; Guo et al., 2020). However, their impacts on surface drag and momentum flux
93 in the midlatitudes are undocumented in the literature. We will demonstrate that di-
94 rectional wave-wind coupling can modulate these surface fluxes, impacting the surface
95 drag and near-surface winds.

96 The three crucial characteristics of the atmospheric fronts relevant to misaligned
97 waves are high winds, abrupt changes in wind direction, and rapid translation. In the
98 warm sector of the fronts, the strong southerly winds force the strongly coupled short
99 wind-waves, generally aligned with the winds. Once the cold front is crossed, the marked
100 shift in the wind direction, combined with the rapid eastward translation, generates a
101 large fetch of growing wind-waves that become quickly misaligned with the northwest-
102 erly winds. Figure 1b illustrates this process schematically. Here, we define that the waves
103 are misaligned with winds when the propagation direction of the most dominant wave
104 differs from the wind direction by $>60^\circ$. Not only is this definition intuitive, but it is
105 also consistent with the observed changes in directional wave spreading across the cold
106 front (not shown).

107 This study identifies and examines the evolutions of misaligned waves under atmo-
108 spheric fronts using direct in-situ surface flux measurements and fully-coupled high-resolution
109 ocean-atmosphere-wave model simulations. A possible modification to more accurately

110 represent the relevant wave-wind physics in the bulk flux parameterization is also dis-
111 cussed. Section 2 describes the observations, parameterizations, and model simulations.
112 Section 3 provides a case study investigation of misaligned waves for one atmospheric
113 front case using model simulations and observations, while Section 4 offers the climato-
114 logical perspectives of the evolution of misaligned waves and their impacts on param-
115 eterized flux using observations. Section 5 concludes the study.

116 **2 Methods**

117 **2.1 Observations**

118 The Pioneer Array, located off the coast of New England and operated by the NSF
119 Ocean Observatories Initiative (OOI, Trowbridge et al., 2019), provides various mete-
120 orological and ocean observations of physical, chemical, and biological processes from De-
121 cember 2014 until November 2022. This study uses the 8-years of near-surface measure-
122 ments of wind, temperature, humidity, and surface wave fields. We also use the momen-
123 tum fluxes from the direct covariance flux system (DCFS), available over a shorter pe-
124 riod (2015-05-13 - 2015-10-23; 2016-05-13 - 2018-03-29; 2018-10-30 - 2019-04-07). NOAA’s
125 National Data Buoy Center (NDBC) buoys off the New England coast are also used, es-
126 pecially surface wave information, including 2D wave spectrum along with significant wave
127 height, dominant wave period, and mean/peak wave direction, co-located with the near-
128 surface measurements of winds, temperature, humidity, pressure, and ocean surface tem-
129 perature.

130 **2.2 SCOAR coupled regional modeling system**

131 We use the Scripps Coupled Ocean-Atmosphere Regional model (SCOAR, Seo et
132 al., 2007, 2014, 2016, 2021; Sauvage et al., 2023), which couples the Weather Research
133 and Forecast model (WRF, Skamarock et al., 2019) in the atmosphere to the Regional
134 Ocean Modeling System (ROMS, Haidvogel et al., 2000; Shchepetkin & McWilliams, 2005)
135 in the ocean and WAVEWATCH III (WW3, Tolman et al., 2002; The WAVEWATCH
136 III Development Group, 2019) for the surface waves. ROMS is driven by the momen-
137 tum, heat, and freshwater fluxes parameterized from COARE3.5 (Fairall et al., 1996, 2003;
138 Edson et al., 2013) implemented in the WRF Mellor-Yamada-Nakanishi-Niino (MYNN)
139 surface layer scheme (Nakanishi & Niino, 2009; Jiménez et al., 2012). ROMS forces WRF

140 by feeding SST and surface current vectors to the WRF surface layer scheme. Between
 141 WRF and WW3, the model offers various wave-to-atmosphere coupling options to de-
 142 termine the surface fluxes, as documented in detail in Sauvage et al. (2023). This study
 143 will examine two particular wave-based roughness length formulations, as described in
 144 Section 2.3. ROMS provides surface current to WW3 to represent the current effect on
 145 waves. WW3 can also be coupled to ROMS to represent energy dissipation due to wave-
 146 breaking and whitecapping. However, the WW3-ROMS coupling is not considered in this
 147 study.

148 2.3 Momentum flux parameterizations

149 The momentum flux (τ), sensible (H_s) and latent (H_l) heat fluxes are parameter-
 150 ized via COARE (Fairall et al., 1996) as:

$$\tau = \rho_a C_D S_r U_r = \rho_a u_*^2, \quad (1)$$

$$H_s = \rho_a C_{pa} C_h S_r \Delta T = -\rho_a C_{pa} u_* T_*, \quad (2)$$

$$H_l = \rho_a L_e C_e S_r \Delta Q = -\rho_a L_e u_* q_*, \quad (3)$$

151 where ρ_a is the air density, C_{pa} is the specific heat capacity of the air at constant
 152 pressure, L_e is the latent heat of evaporation, T is the potential temperature, Q is the
 153 water vapor mixing ratio, S_r is the scalar averaged wind speed relative to the ocean sur-
 154 face, U_r is the magnitude of the wind vector relative to the ocean surface, C_D , C_h , C_e
 155 are the transfer coefficients for stress, sensible and latent heat, and u_* , T_* , q_* are the Monin-
 156 Obukhov similarity scaling parameters. The drag coefficient C_D is defined as:

$$C_D(z, z_0, \psi_m) = \left[\frac{\kappa}{\ln(z/z_0) - \psi_m(\zeta)} \right]^2, \quad (4)$$

157 where κ is the von Kármán constant, $\psi_m(\zeta)$ is an empirical function of atmospheric
 158 stability, ζ is the z/L ratio with L the Obukhov length and z the height above the sur-
 159 face. The COARE wave-based formulation (Edson et al., 2013) parameterizes the wave-
 160 induced surface roughness (z_0^{rough} , hereafter simply z_0) as,

$$z_0 = H_s D \left(\frac{u_*}{c_p} \right)^B, \quad (5)$$

161 where H_s is the significant wave height, u_*/c_p is the inverse wave age based on u_* , and
 162 the peak phase speed of the wave (c_p). D and B are numerical constants given by $D =$

163 0.09 and $B = 2$ (Edson et al., 2013). In addition to Eq. 5 included in the COARE3.5
 164 public release, Sauvage et al. (2023) tested a revised formulation, in which z_0 increases
 165 as the wave-wind misalignment increases (Porchetta et al., 2019, 2021),

$$z_0 = H_s D \cos(a\theta) \left(\frac{u_*}{c_p}\right)^{B \cos(b\theta)}, \quad (6)$$

166 where θ is the absolute directional difference between the 10-m wind and the peak wave
 167 direction. D and B are the same coefficients as in Eq. 5, while the coefficients $a = 0.45$
 168 and $b = -0.32$ are determined by Porchetta et al. (2019) from a set of midlatitude off-
 169 shore in situ measurements, including the Air-Sea Interaction Tower (ASIT) south of Martha’s
 170 Vineyard, which is close to the region of the current study.

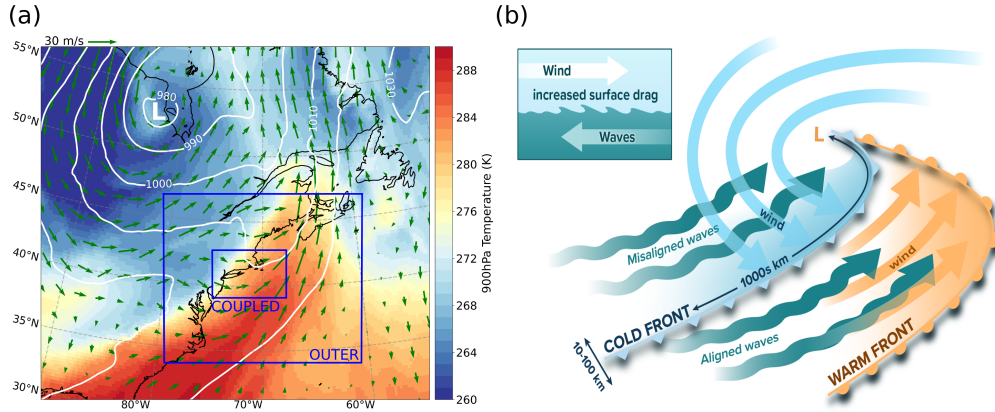


Figure 1. (a) An extratropical cyclone in the North Atlantic on December 6, 2017, at 12:00 UTC, showing the potential temperature at 900 hPa (K), overlaid with the mean sea level pressure (contours, hPa) and the 900 hPa wind (arrows), from the ERA5 reanalysis. The extent of the outer and nested model domains is also indicated. (b) A schematic representation of an atmospheric front passing over the ocean showing aligned wind-waves under the warm sector and strongly misaligned waves behind the cold front. The schematic at the top left represents the mechanism of the enhanced drag behind the cold front when wind and waves are misaligned. The "L" symbol denotes the center of the low-pressure system in both (a,b).

171 2.4 Experiments

172 The model domain covers the North Atlantic (Figure 1a) with a nested configura-
 173 tion. In the outer domain, the model is run at 7.5 km resolution and is atmosphere-
 174 only, dynamically downscaling the large-scale atmospheric circulation with spectral nudg-

175 ing. This drives the inner domain zooming over the US Northeast (Figure 1a), where WRF,
 176 ROMS, and WW3 are fully coupled at an hourly frequency and run at the identical 1.5
 177 km resolution with matching grids and land-sea masks. ROMS has 30 vertical levels with
 178 a stretched vertical grid that enables the enhanced resolutions near the surface and the
 179 bottom, with $\theta_s = 7.0$, $\theta_b = 0.1$, and $h_{cline} = 300$ m, yielding a minimum of 15 layers in
 180 the upper 150 m. The vertical resolution of WRF is refined to have 50 vertical levels with
 181 ≈ 20 levels below 250 m. The lowest level is close to the surface (5.5 m), with the 2nd
 182 lowest level at 12 m per Shin et al. (2012).

183 In WRF, deep cumulus convection is represented through the Multi-scale Kain-Fritsch
 184 scheme (Zheng et al., 2016), the cloud micro-physics by the WRF single-moment 6-class
 185 scheme (Hong & Lim, 2006), the land surface process by the Noah land surface model
 186 (F. Chen & Dudhia, 2001), and the Rapid Radiative Transfer Model for general circu-
 187 lation models (RRTMG, Iacono et al., 2008) for the shortwave and longwave radiations.
 188 The planetary boundary layer (PBL) processes are treated with the MYNN level 2.5 scheme
 189 (Nakanishi & Niino, 2009). In ROMS, the KPP (K profile parameterization) scheme (Large
 190 et al., 1994) determines vertical eddy viscosity and diffusivity. In WW3, the ST6 pack-
 191 age is used to parameterize wind input, wave breaking, and swell dissipation (Babanin,
 192 2011; Stopa et al., 2016; Liu et al., 2019). Nonlinear wave-wave interactions are com-
 193 puted using the discrete interaction approximation (Hasselmann et al., 1985). Reflec-
 194 tion by shorelines is enabled through the Arduin and Roland (2012) scheme. The depth-
 195 induced breaking is based on Battjes and Janssen (1978), and the bottom friction for-
 196 mulation follows Arduin et al. (2003).

197 Two coupled model simulations are run for a 3-day case study (December 5-8, 2017)
 198 featuring one passing atmospheric front (Figure 1a). In the simulation dubbed *WBF θ* ,
 199 the roughness length is parameterized by Eq. 6, where the wind and wave misalignment
 200 effect is considered. This will be compared to another simulation, called *WBF*, where
 201 such an effect is omitted (Eq. 5). In both simulations, the WRF model is initialized and
 202 driven by the 1-hr 0.25° ERA5 reanalysis (Hersbach et al., 2020), ROMS by the daily
 203 $1/12^\circ$ MERCATOR International global reanalysis (Lellouche et al., 2018), and WW3
 204 by 11 spectral points obtained from the global $1/2^\circ$ WW3 simulations (Rascle & Ar-
 205 duin, 2013). The initial conditions for WW3 were obtained from the 30-day spin-up sim-
 206 ulations forced by ERA5 atmospheric forcing. In ROMS, the tidal forcing is obtained
 207 using the Oregon State University Tidal Prediction Software (Egbert & Erofeeva, 2002)

208 and applied as a 2-D open boundary condition by prescribing the tidal period, elevation
 209 amplitude, current phase angle, current inclination angle, the minimum, and maximum
 210 tidal current, and ellipse semi-minor axes for 13 major tidal constituents (Steffen et al.,
 211 2023).

212 3 Case Study Examination

213 This section uses in situ observations and model simulations to examine the mis-
 214 aligned waves during one atmospheric front. To provide spatial context, we will discuss
 215 the model results first. Figure 2 compares three stages of a cold front passage, showing
 216 the directional misalignment (θ) and the wind-speed-based wave age ($\chi = c_p/U_{10}$) for
 217 three different times: December 6 at 09:00 UTC, when the Pioneer Array is ahead of the
 218 cold front (pre-cold-front), at 12:00 UTC (cold-front), and at 15:00 UTC (post-cold-front).
 219 Hereafter, U_{10} is defined as $U_{10} = (U_{10x}^2 + U_{10y}^2)^{1/2}$ where U_{10x} is the zonal and U_{10y}
 220 is the meridional wind components.

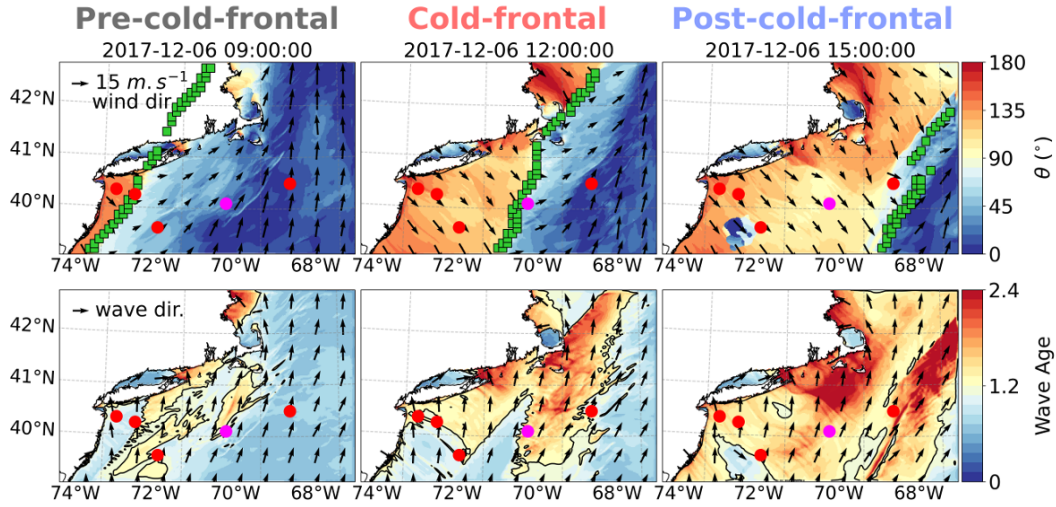


Figure 2. The top row shows the evolution of θ (shading), overlaid with the surface wind (black arrows) as simulated from the WBF θ run at 09:00 (pre-cold-front), 12:00 (cold-front) and 15:00 (post-cold-front) UTC on December 6, 2017. The green markers indicate the detected cold front using the Parfitt et al. (2017) algorithm. The bottom row shows the evolution of the wave age, overlaid with the wave peak direction (normalized black arrows). A wave age of 1.2 is indicated by a black contour. The magenta circle denotes the location of the Pioneer Array, and the 4 red circles are the NDBC moorings (from left to right: mooring identification numbers 44065, 44025, 44066, and 44008).

221 3.1 Evolutions of winds and waves

222 During the pre-cold-front, the directional misalignment is generally small ($\theta < 45^\circ$).
 223 The strong southerly and southwesterly wind (black vectors in the top row) in the warm
 224 sector is associated with the southerly waves (black vectors in the bottom row), with an
 225 overall developing sea state ($\chi < 1.2$). The wind abruptly switches to northwesterly
 226 across the cold front. In response, strongly misaligned waves with $\theta > 100^\circ$ occur over
 227 a broad fetch west of the cold front, with χ rising above 1.2. As the front moves east-
 228 ward, a new area of misaligned waves is continuously generated in the far east, with the
 229 developing sea state ($\chi < 1.2$) progressively turning into a mixed sea state ($1.2 < \chi <$
 230 3) in the far west. Much of the sea state behind the cold front is a mixture of two wave
 231 categories: slightly older southerly wind waves forced by the warm sector southerly wind
 232 and newly generated younger short wind waves forced by the cold sector northwesterly
 233 wind (Figures 2 and 3).

234 These wind and wave evolutions from the model are consistent with the observa-
 235 tions at the Pioneer Array. Figure 3 shows the hourly time series of the near-surface me-
 236 teorological and wave measurements. During the pre-cold-front (gray-shaded period),
 237 southerly winds (black arrows) with >10 m/s and a developing sea state ($\chi \leq 1.2$) were
 238 observed. The waves were largely aligned with the wind (red arrows). After the cold front
 239 passage on December 6 at 12:00 UTC (red-shaded period), the near-surface air temper-
 240 ature and relative humidity dropped rapidly, and the wind direction switched to north-
 241 westerly, while the dominant wave direction continued to be southerly, indicating a large
 242 degree of wave-wind misalignment ($\theta \geq 100^\circ$) and a mixed sea state ($\chi > 1.2$). For
 243 this particular event, the wind waves remained misaligned with the winds for more than
 244 18 hours after the cold front, after which the waves gradually became aligned with the
 245 wind, and the wave age subsided below 1.2.

246 The adjacent NDBC buoys captured similar wave responses. The 2D wave spec-
 247 tra plots constructed from the 4 NDBC buoys (Figure 4) indicate that during the pre-
 248 cold-front, the dominant wave direction is southerly, with wave periods of 5-10s. Even
 249 after the cold front passes, these southerly surface waves persist, while new short waves
 250 with a period lower than 5s are generated from the northwest. While there is a reason-
 251 able range of regional variability across the buoys, the salient feature of the wave responses
 252 is broadly consistent across all the buoys examined. Compared to the Pioneer Array and

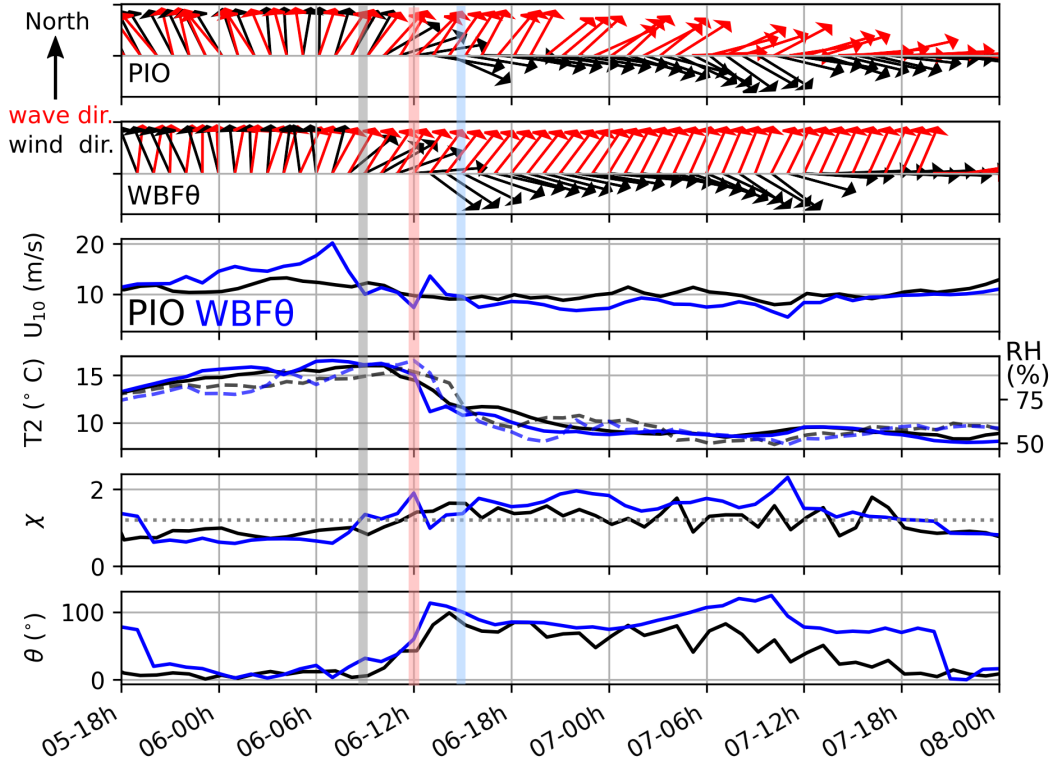


Figure 3. The top two panels show the observed and simulated (WBF θ) wind direction (black arrows) and wave peak direction (red arrows) around the passing of the atmospheric front on December 6, 2017. The length of the arrows in the top two panels is normalized. Gray, red, and blue shaded periods denote the pre-cold-front, cold-front, and post-cold-front shown in Figure 2. The following panels show the 10 m wind speed (U_{10} , m/s), air temperature (T2, solid line, °C), relative humidity (RH, dashed line, %), wave age, and misalignment angle (θ , °) from the Pioneer Array (black) and WBF θ (blue). The dotted gray line on the wave age panel denotes the wave age = 1.2.

253 the NDBC buoys, the simulation (WBF θ) also captures the characteristics of the atmo-
 254 spheric front and the observed wave evolution reasonably well. The model also captures
 255 the background easterly swell observed from the NDBC buoys.

256 Figure 5 shows the frequency-averaged wave energy density spectra (E_f) during
 257 the passage of the atmospheric front in WBF θ . The top row shows the average energy
 258 coming from the 90° sectors from the southwest to southeast direction, while the bot-
 259 tom row shows the energy coming from the 90° sectors from the west to north direction.
 260 Strong southerly wave energy builds under the warm sector ahead of the cold front and

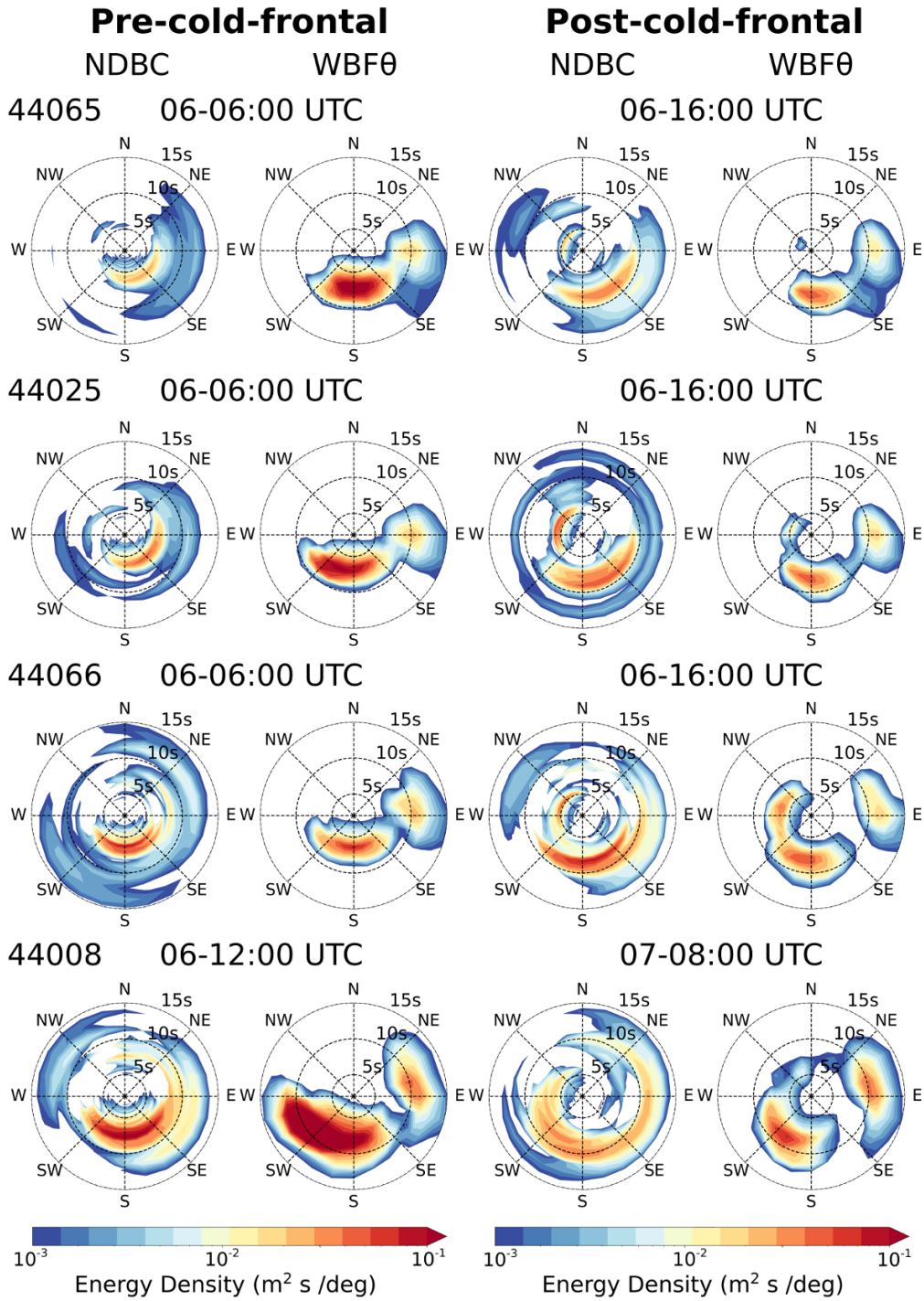


Figure 4. The 2D wave energy density spectra ($m^2 s / \text{deg}$) shown in the period space calculated from the 4 NDBC mooring locations, 44065, 44025, 44066, and 44008 (see Figure 2 for mooring locations) and the WBFθ run during a pre-cold-front (left column) and post-cold-front (right column) time.

261 dissipates as the cold front passes over the region. Meanwhile, the northwesterly winds
 262 behind the cold front generate new waves coming from the northwest, so the wave en-
 263 ergy from that direction grows following the cold front, creating mixed sea conditions.
 264 Note that the color scale on Figure 5 is different on both rows and indicates that the southerly
 265 energy is much stronger and dominant even after the cold front, leading to the observed
 266 wind and wave misalignment. As suggested in Figure 3, more than 18 hours after the
 267 passage of the cold front is needed for the waves to be aligned again and for the southerly
 268 wave energy under the warm sector to dissipate eventually.

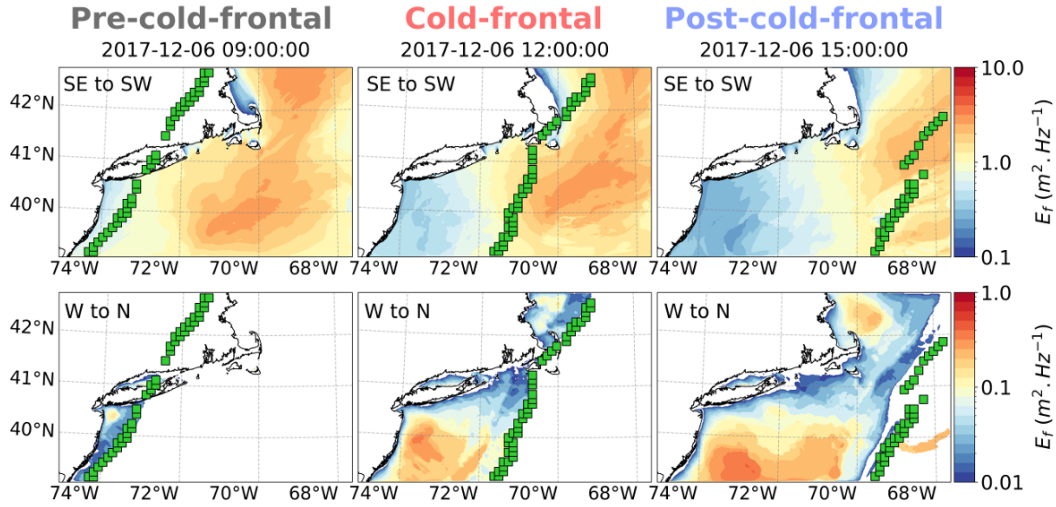


Figure 5. The frequency-averaged wave energy density spectra ($E_f, m^2.Hz^{-1}$) as simulated from the WBF θ run at 09:00 (pre-cold-front), 12:00 (cold-front) and 15:00 (post-cold-front) UTC on December 6, 2017. The green markers indicate the detected cold front using the Parfitt et al. (2017) algorithm. The top row shows the energy coming from the 90° sector from the southeast to southwest direction (SE to SW), while the bottom row shows the energy coming from the 90° sector from the west to north direction (W to N).

269 3.2 Impacts on surface drag and momentum flux

270 The WBF θ run is compared with the WBF run to reveal the effect of misaligned
 271 waves. For this, we will focus on differences in directly impacted variables: z_0 , C_D , τ ,
 272 and wind speeds at two different heights, 10 m (within the surface layer, U_{10}) and 110
 273 m (above the surface layer, U_{110}). We will also discuss the changes in turbulent heat flux

274 after that. For simplicity, we will compare the difference only at the post-cold-front (De-
 275 cember 6, 15:00 UTC).

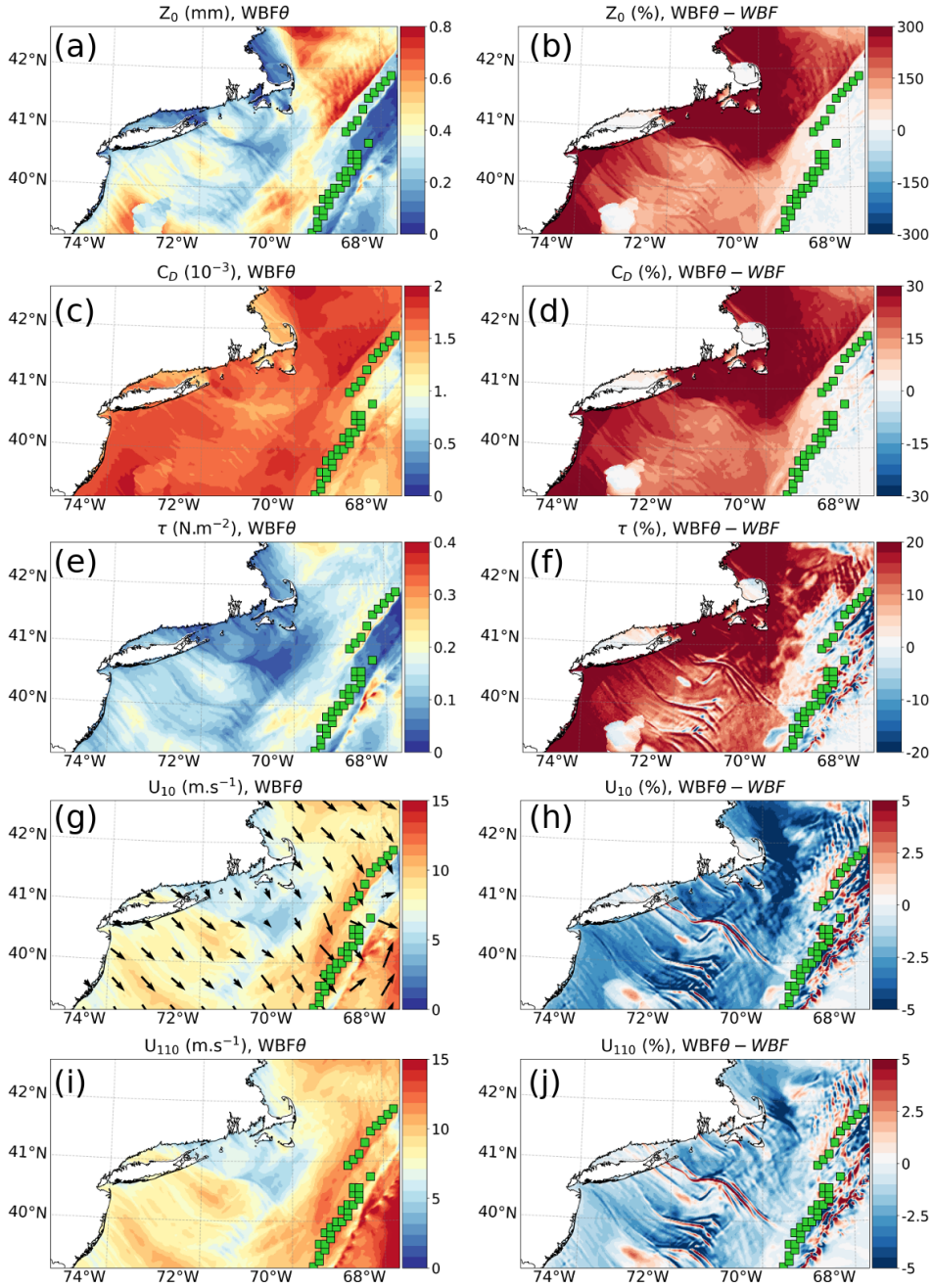


Figure 6. (a,c,e,g,i) shows the roughness length (z_0), drag coefficient (C_D), momentum flux (τ), surface wind speed (U_{10}) and wind speed at 110 m (U_{110}) from WBF θ and (b,d,f,h,j) the percent difference between WBF θ and WBF (%) after the passage of the cold front, at 15:00 UTC on December 6, 2017. The arrows overlaid on U_{10} indicate the direction of the surface wind. The green markers indicate the detected cold front using the Parfitt et al. (2017) algorithm.

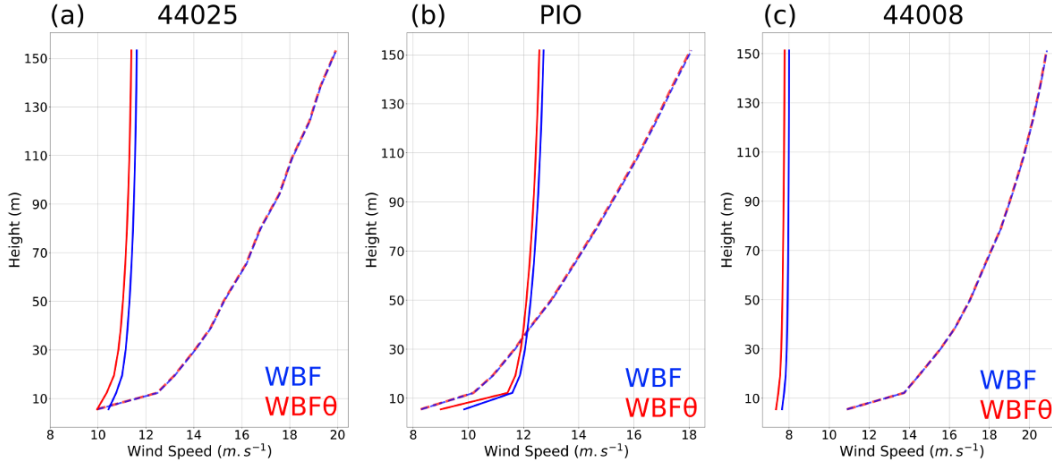


Figure 7. Vertical wind speed profiles from WBF (blue) and WBF θ (red) at (b) Pioneer Array location and (a,c) two NDBC moorings, 44025 and 44008. On each plot, a profile before (dashed) and a profile after (solid) the passage of the cold front is shown. For NDBC moorings (a,c), the times are chosen to be the same as in Figure 4, while for Pioneer Array (b), the times are chosen to be the pre-cold-front and post-cold-front shown in Figure 2.

276 The left column of Figure 6 shows WBF θ , and the right column shows the differ-
 277 ence between WBF θ and WBF, expressed as the percentage difference ($(\text{WBF}\theta - \text{WBF})$
 278 $/ \text{WBF}) \times 100$). East of the cold front, where the wave and wind are largely aligned, lit-
 279 tle difference is found in each of these four quantities. However, sizable increases are found
 280 in z_0 , C_D , and τ west of the cold front. The increase can be as high as 300% for z_0 , 30%
 281 for C_D , and 20% for τ , respectively. If area-averaged over the broad region west of the
 282 cold front, the increases are 185.7%, 19.3%, and 11%, respectively (Fig. 6a-d). Moreover,
 283 because of the increase in the surface drag, U_{10} is reduced in WBF θ by up to 5% (or 2%
 284 when area-averaged, Fig. 6g,h). The increased drag by the misaligned wave is also felt
 285 above the surface layer. Here, the wind at 110 m is chosen to show the impact above the
 286 surface layer (Figure 6i,j). U_{110} is reduced behind the cold front, having a coherent spa-
 287 tial pattern to that of U_{10} . However, the magnitude of the reduction above the surface
 288 layer is generally small (1-5% or $0.1\text{-}0.5 \text{ m.s}^{-1}$, Figure 6i,j). Figure 7 shows wind speed
 289 profiles at different NDBC moorings and Pioneer Array locations, confirming that the
 290 effect of increased drag by the misaligned waves on wind speed is largest in the surface
 291 layer and smaller above it.

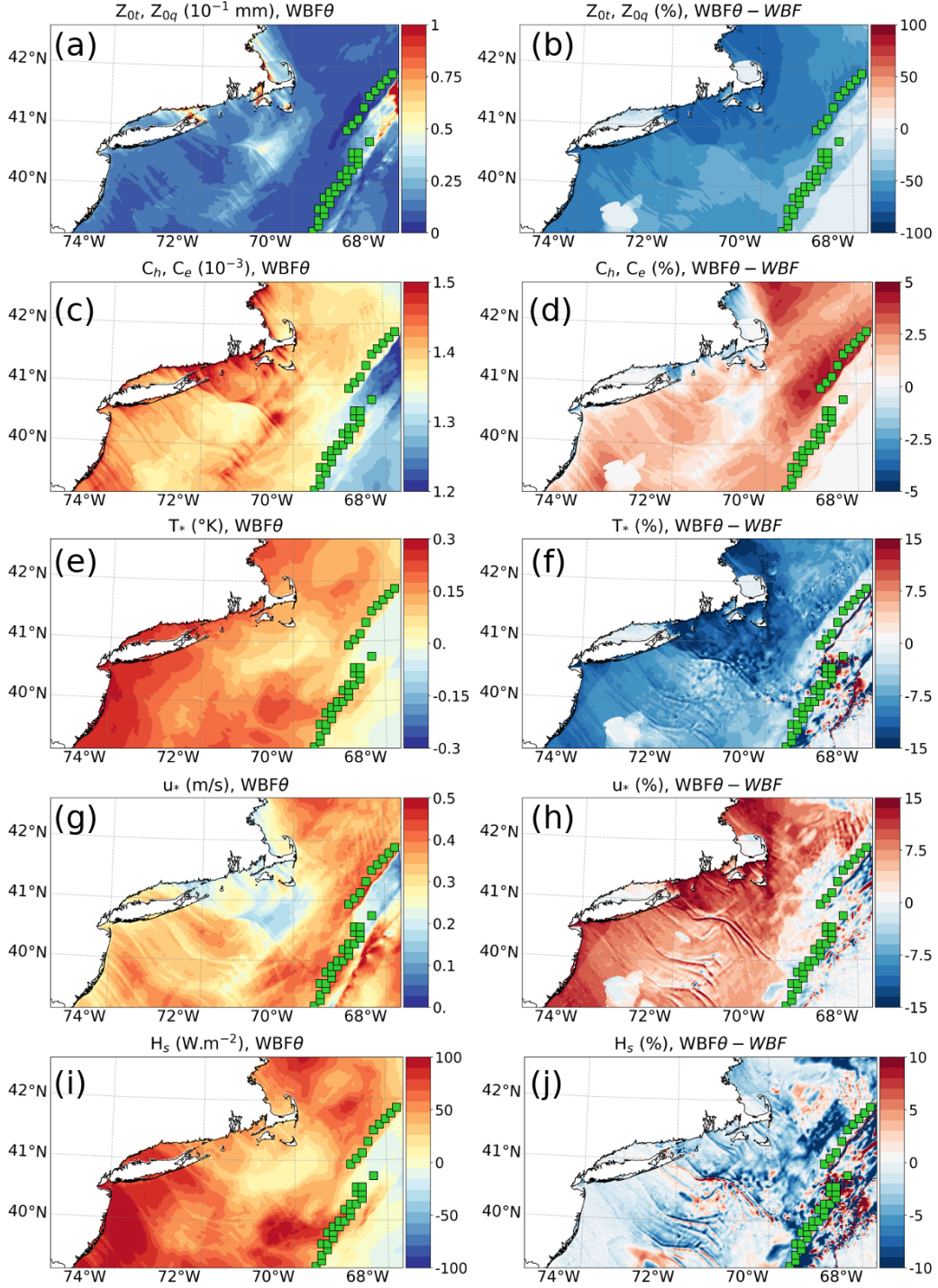


Figure 8. As in Figure 6, but for the scalar roughness length ($z_{0t}, z_{0q}, 10^{-1}mm$), the exchange coefficient for heat and moisture ($C_h, C_e, 10^{-3}$), the temperature scaling parameter (T_* , °K), the friction velocity (u_* , $m.s^{-1}$) and the sensible heat flux ($H_s, W.m^{-2}$). Heat flux is defined as positive upward.

292

3.3 Impacts on turbulent heat flux

293

294

295

296

297

298

299

300

301

302

303

304

305

The increases in surface roughness length due to misaligned waves also modify the upward sensible heat flux (H_s) and latent heat flux (H_l), reducing them west of the cold front by up to 10% (2.5% when area-averaged, Figure 8i,j and Figure 9c,d). This decrease in upward turbulent heat fluxes occurs despite a moderate increase in the exchange coefficients for heat and moisture (respectively C_h and C_e ; note that these are equal in the COARE3.5 algorithm) by up to 5% (Figure 8c,d). To investigate in more detail the impact on heat fluxes, based on WRF outputs from WBF and WBF θ and using COARE3.5 offline, we re-calculated the scalar roughness length for temperature and humidity (z_{0t} and z_{0q}), the surface exchange coefficients (C_h and C_e) and the specific humidity scaling parameter (q_*) which are not directly given by WRF outputs. Comparing the implementation of COARE3.5 in the MYNN surface scheme (Olson et al., 2021) to the COARE3.5 offline version, we are confident that the result would be the same if taken directly from WRF. z_{0t} is defined using the roughness Reynolds number (R_r) as:

$$R_r = \frac{u_* z_0}{\nu}, \quad (7)$$

$$z_{0t} = \frac{5.8e^{-5}}{R_r^{0.72}}, \quad (8)$$

306

307

308

where ν is the kinematic viscosity of the air. In COARE3.5, the moisture roughness length z_{0q} is equal to z_{0t} . The sensible and latent heat transfer coefficients are defined as

$$C_h(z, z_0, z_{0t}, \psi_m, \psi_h) = \left[\frac{\kappa}{\ln(z/z_0) - \psi_m(\zeta)} \right] \left[\frac{\kappa}{\ln(z/z_{0t}) - \psi_h(\zeta)} \right], \quad (9)$$

$$C_e(z, z_0, z_{0q}, \psi_m, \psi_h) = \left[\frac{\kappa}{\ln(z/z_0) - \psi_m(\zeta)} \right] \left[\frac{\kappa}{\ln(z/z_{0q}) - \psi_h(\zeta)} \right], \quad (10)$$

309

310

where $\psi_h(\zeta)$ is another empirical function of atmospheric stability. Because $z_{0q} = z_{0t}$ in COARE3.5, $C_e = C_h$.

311

312

313

314

The scalar roughness length z_{0t} is inversely proportional to the velocity roughness length z_0 , so an increase in z_0 due to wave misalignment (Fig. 6a,b) drives a decrease in z_{0t} (60% when area-averaged, Figure 8a,b). This increased resistance to turbulent scalar transport decreases the magnitude of the turbulent flux scale for temperature, T_* , by up

315 to 15%, Figure 8e,f. Note that T_* and the turbulent moisture flux scale q_* are defined
 316 to be negative for heat fluxes out of the ocean, so we plot $-T_*$ and $-q_*$ so that positive
 317 values of these quantities correspond to positive values of H_s and H_l . Overall, in Eq. 2,
 318 the increase in u_* due to misalignment (Figure 8g,h) is more than offset by the decrease
 319 in $-T_*$, resulting in a small decrease in sensible heat flux. Similarly, the decrease in z_{0q}
 320 induces a decrease in $-q_*$, which compensates for the increase in u_* and results in a small
 321 decrease in H_l overall, Equation 3 and Figure 9.

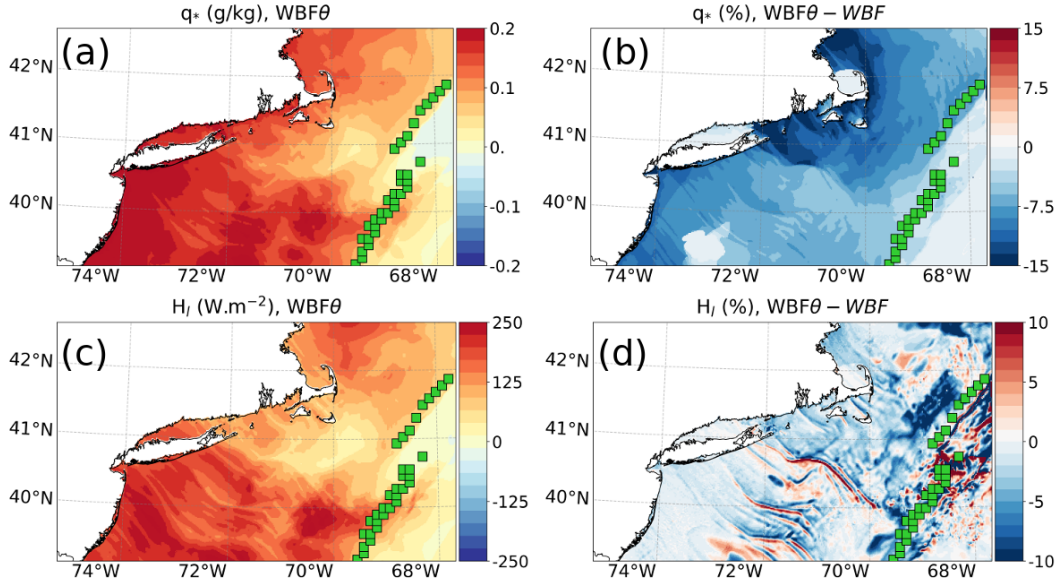


Figure 9. As in Figure 6 but for (a,b) the specific humidity scaling parameter (q_* , g/kg) and (c,d) the latent heat flux (H_l , $W.m^{-2}$).

322 4 Long-term characterization

323 Multi-year measurements of near-surface meteorology, surface waves, and direct co-
 324 variance fluxes from the Pioneer Array are used to examine the long-term characteris-
 325 tics of the misaligned waves under cold fronts. To do that, we first have to detect the
 326 cold front from the buoys. Because surface-based observations are used, the detected fronts
 327 can be deemed surface cold fronts. Here, we use the meridional surface wind (U_{10y}) and
 328 the 2-m air temperature (T_2). The cold front is identified when U_{10y} is shifted from southerly
 329 to northerly, with an additional criterion that the northerly (southerly) U_{10y} must per-
 330 sist over 2 hrs after (before) the frontal passage. We then check for a decrease in T_2 by
 331 $>3^\circ\text{C}$ between $t=-2$ hrs and $t=+8$ hrs. To ensure a strong shift in wind direction at the

332 passage of the cold front, we also require a change in wind direction of at least 60° . If
 333 all these conditions are met, the event is considered an atmospheric cold front over the
 334 Pioneer Array at $t=0$. Using this set of criteria, 86 atmospheric cold fronts were iden-
 335 tified from the 8-year Pioneer Array dataset. 55 of these events have co-located measure-
 336 ments of surface waves, which are used for subsequent analysis. Hereafter, we defined
 337 misaligned waves when the angle between wind and waves exceeds at least 60° . The re-
 338 sults presented here do not change appreciably with reasonable variations of criteria.

339 Figure 10a shows the histogram of the so-detected cold front occurrence as a func-
 340 tion of calendar months. Consistent with the previous studies (Parfitt et al., 2017; Reeder
 341 et al., 2021), the cold fronts are most frequently observed during the extended winter
 342 period (November - March), with 62 out of 86 events. Figure 10b shows the composite
 343 evolutions of θ across the fronts, indicating strongly misaligned waves at the cold front
 344 passage ($t=0$).

345 These fronts feature southerly wind (Figure 10c) with moderate speed (8 m/s, Fig-
 346 ure 10d) in the warm sector accompanied by a strong shift in wind direction from the
 347 warm to cold sectors exceeding at least 60° (Figure 10c). Because of moderate wind con-
 348 ditions in the warm sector, the sea state is generally characterized by a mixed sea ($1.2 <$
 349 $\chi < 2$), where wind-waves and some pre-existing swell co-exist, the condition that was
 350 also observed from the NDBC buoys (Figure 4). As the cold front passes and the winds
 351 change direction, the waves begin to be misaligned 1~2 hrs before the front, and once
 352 generated, the waves remain misaligned for 8 hours on average (Figure 10b).

353 We use the DCFS momentum flux measurements at the Pioneer Array to evalu-
 354 ate the accuracy of the parameterized momentum flux. Because DCFS data are avail-
 355 able for a shorter period (see Section 2.1), only 36 atmospheric front events were iden-
 356 tified from this period, of which 20 have led to misaligned waves ($\theta > 60^\circ$). Figure 11a,b
 357 shows the composite evolutions of the directly measured C_d and τ (black) for the fronts
 358 that generated the misaligned waves. With the state variables measured from the Pi-
 359 oneer Array, we then calculated C_d and τ without misaligned waves (blue, Eq. 5) and
 360 with misaligned waves (red, Eq. 6). The result shows that the estimated momentum flux
 361 with misaligned waves is higher than without by 16.5% at $t=0$ and 6.6% for 8 hours af-
 362 ter the cold front. When averaged over the 8 hours after the cold front, this elevated wind
 363 stress with misaligned waves is closer to the DCFS estimates (bias is reduced from 4.9%

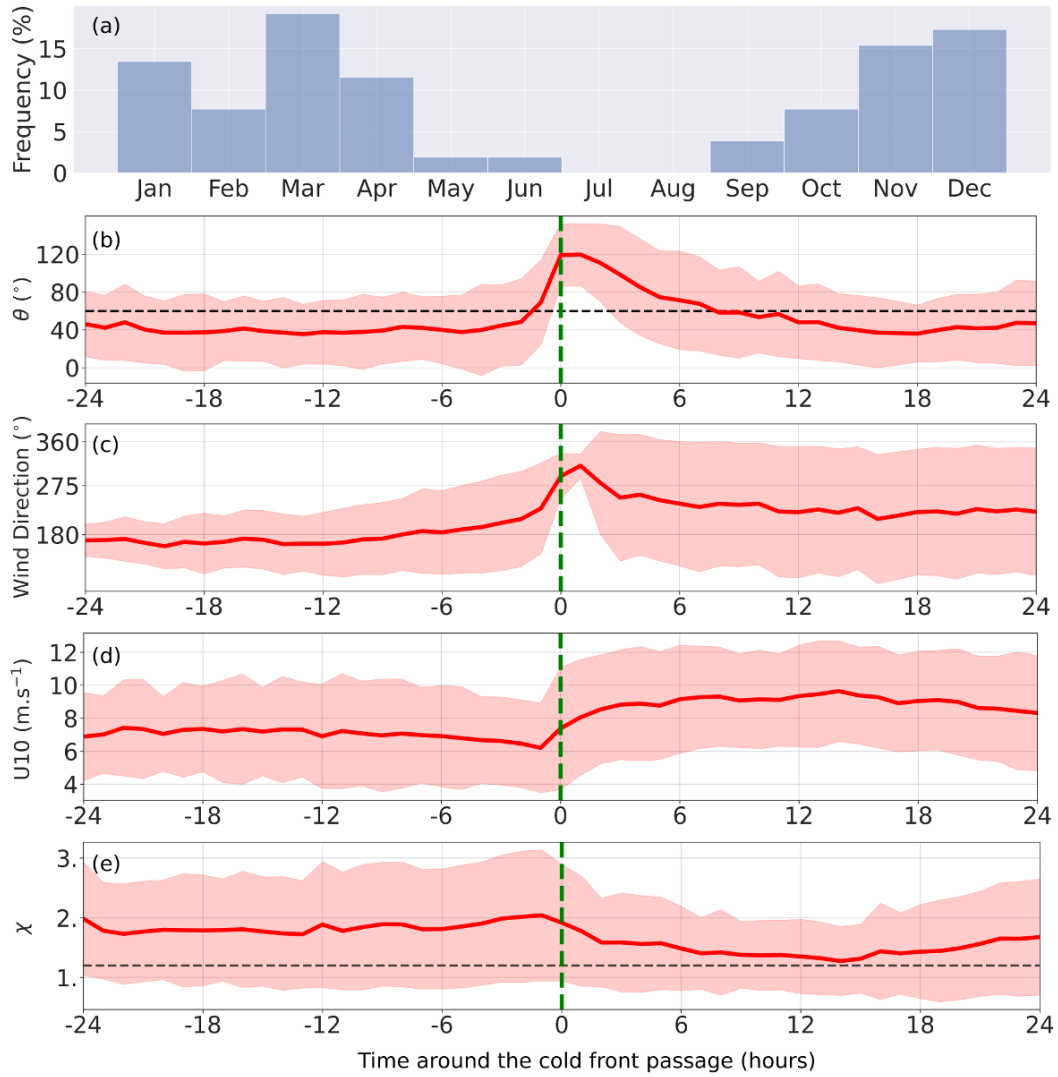


Figure 10. (a) Probability of occurrence of cold front per month (%) calculated using the Pioneer Array data from December 2014 to November 2022. (b,c,d,e) Composite evolutions of (b) misalignment angle (θ , $^{\circ}$), (c) wind direction ($^{\circ}$, 0 means northerly), (d) wind speed (m/s), and (e) wave age for the detected atmospheric cold fronts. The shaded envelopes represent ± 1 standard deviations. In (b), the dashed line indicates the 60° line; in (e), a wave age 1.2. The vertical green line indicates the cold front at a $t=0$.

364 to 1.1% for τ and from 6% to 1.1% for C_d). The results also corroborate the modeling
 365 results (WBF vs. WBF θ).

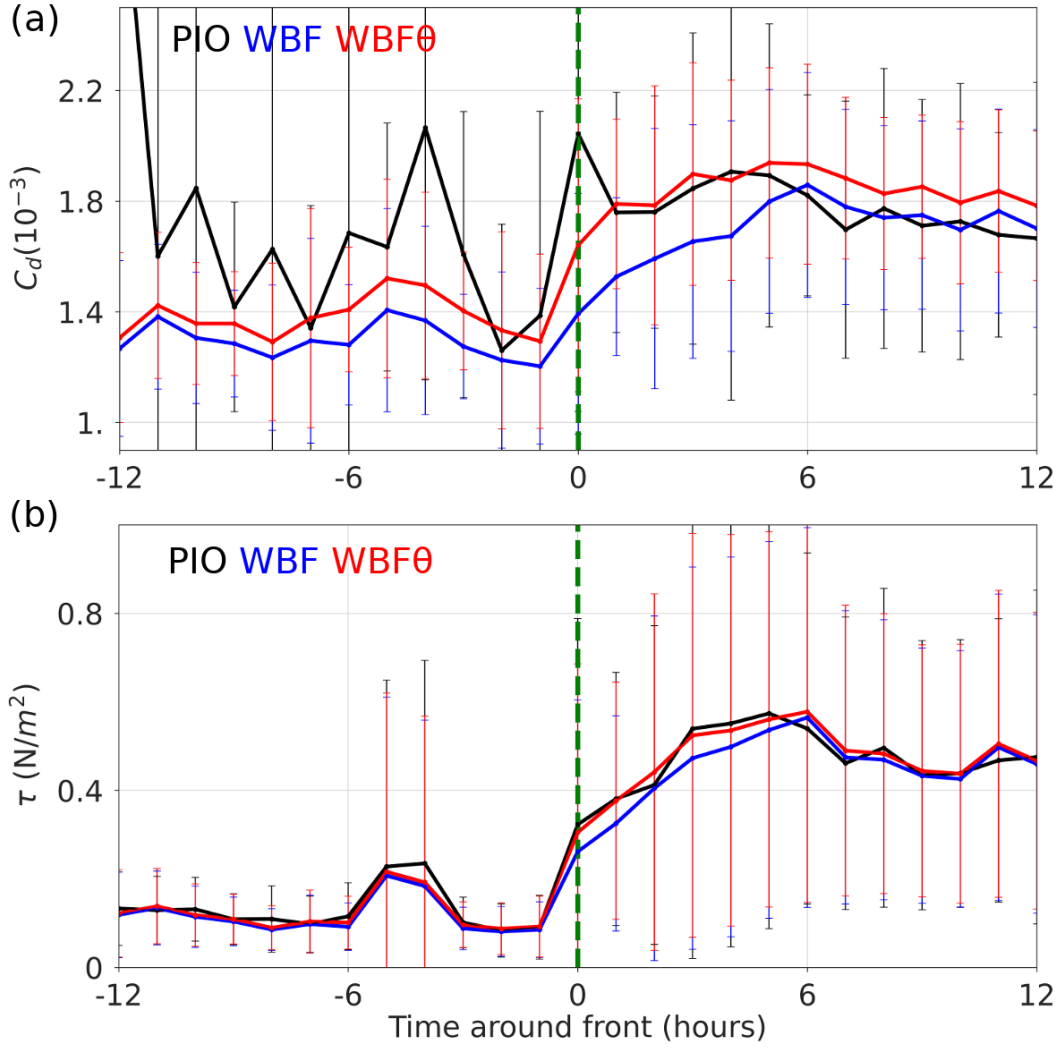


Figure 11. Composite evolution of the parameterized (a) drag coefficient ($C_d, 10^{-3}$) and (b) momentum flux (τ, Nm^{-2}) calculated offline using the COARE3.5 (WBF θ , red) with and (WBF, blue) without the misaligned wave effect, in comparison to direct covariance flux measurements from the Pioneer Array (PIO, black). The error bars represent ± 1 standard deviation. The vertical green line indicates the cold front at $t=0$.

366 **5 Conclusion and Discussions**

367 Using the multi-year in-situ observations and numerical model simulations, this study
 368 examined the nature and impacts of the misaligned surface waves behind the passing of
 369 atmospheric cold fronts off the coast of New England. A case study investigation indi-
 370 cates that an atmospheric cold front generates a significant fetch of misaligned waves be-
 371 hind it, comparable to the lateral extent of the extratropical cyclones in which the front

372 is embedded. Over a vast region of misaligned waves propagating with the front, the model
 373 simulations indicate that misaligned waves significantly increase the roughness length,
 374 drag and enthalpy exchange coefficients, and wind stress. In response to increased sur-
 375 face drag, the near-surface wind speed is reduced, reducing upward turbulent heat fluxes.
 376 Note that the decrease in upward turbulent heat flux is despite the moderate increase
 377 in surface heat and moisture exchange coefficients. Indeed, the scalar roughness decreased
 378 as the velocity roughness increased, decreasing the temperature and humidity scaling pa-
 379 rameters and increasing the friction velocity. This leads to compensating effects on both
 380 latent and sensible heat fluxes. Hence, the magnitudes of the responses in turbulent heat
 381 fluxes are modest.

382 The long-term analysis using the Pioneer Array data allowed us to detect over 50
 383 atmospheric cold fronts, which generated misaligned waves behind them. Once gener-
 384 ated, these waves remain misaligned with the wind for 8 hours on average. This percent-
 385 age of atmospheric cold front detection, of course, depends on the chosen threshold, but
 386 the results are qualitatively similar.

387 The current COARE wave-based bulk flux parameterization assumes that waves
 388 and wind are aligned (Eq. 5). A simple modification to this formulation is suggested to
 389 represent the misaligned wave effect as in Eq. (6), which produces overall improved es-
 390 timates of the parameterized momentum flux under this condition. As discussed exten-
 391 sively in Sauvage et al. (2023), equivalent to incorporating the directional misalignment
 392 in COARE is simply replacing the peak wave period with the mean wave period to cal-
 393 culate the wave age in Eq. (5) (See their Eq. 12). The rationale is that the spectrally-
 394 averaged wave period more accurately depicts a sea state that is a mixture of wind waves
 395 of ranging frequencies, as in Figure 4.

396 Finally, the impacts of the improved surface stress on the wind profile appear lim-
 397 ited to the surface layer. An important caveat to consider is that the present analysis
 398 mainly concerns the “instantaneous” impacts of the altered momentum flux, whereas,
 399 in the nature and long-term coupled runs, the mixed layer depth will likely respond to
 400 different turbulent momentum and heat fluxes, thereby greatly affecting state variables
 401 such as sea surface temperature. These effects cannot be captured in the short 3-day sim-
 402 ulations. Longer simulations that fully resolve the interactions between the atmospheric
 403 fronts and surface waves are needed to determine the impacts on kinematic and ther-

404 modynamic properties in the PBL and upper ocean and possibly the evolution of the at-
405 mospheric fronts.

406 **6 Open Research**

407 ERA5 data are made available by Copernicus Climate Change Service (<https://>
408 cds.climate.copernicus.eu), Mercator by Copernicus Marine Environment Monitor-
409 ing Service (<https://doi.org/10.48670/moi-00016>), and global 3-hourly spectral wave
410 analyses by Ifremer (<ftp://ftp.ifremer.fr/ifremer/ww3/HINDCAST/GLOBAL>). OOI Pi-
411 oneer Array data are obtained from <https://dataexplorer.oceanobservatories.org>,
412 and NDBC data from <https://www.ndbc.noaa.gov/>. WW3 is distributed via <https://>
413 github.com/NOAA-EMC/WW3, WRF <https://github.com/wrf-model/WRF>, and ROMS <https://>
414 www.myroms.org/. The SCOAR codes are available via <https://github.com/SCOAR-model/>
415 SCOAR. The modified COARE3.5 code is available at <https://github.com/cesarsauvage/>
416 COARE3.5_modified_Sauvage-et-al..2023 and the model outputs at Zenodo.

417 **Acknowledgments**

418 This research was supported by NOAA (NA19OAR4310376), NASA (80NSSC21K1524),
419 NSF (OCE-2148120), and DOE (DE-EE0009424). Additionally, HS acknowledges NSF
420 (OCE-2022846). The WHOI High-Performance Computing Facility provided the com-
421 puting resources.

References

- 422
- 423 Arduin, F., O'Reilly, W. C., Herbers, T. H. C., & Jessen, P. F. (2003). Swell
424 Transformation across the Continental Shelf. Part I: Attenuation and Direc-
425 tional Broadening. *Journal of Physical Oceanography*, *33*(9), 1921–1939. doi:
426 10.1175/1520-0485(2003)033<1921:STATCS>2.0.CO;2
- 427 Arduin, F., & Roland, A. (2012). Coastal wave reflection, directional spread,
428 and seismoacoustic noise sources. *Journal of Geophysical Research: Oceans*,
429 *117*(C11). doi: 10.1029/2011JC007832
- 430 Babanin, A. (2011). *Breaking and Dissipation of Ocean Surface Waves*. Cambridge:
431 Cambridge University Press. doi: 10.1017/CBO9780511736162
- 432 Battjes, J. A., & Janssen, J. P. F. M. (1978). Energy Loss and Set-Up Due
433 to Breaking of Random Waves. *Coastal Engineering*, 569–587. doi:
434 10.1061/9780872621909.034
- 435 Berry, G., Reeder, M. J., & Jakob, C. (2011). A global climatology of atmospheric
436 fronts. *Geophysical Research Letters*, *38*(4). doi: 10.1029/2010GL046451
- 437 Bjerknes, J., & Solberg, H. (1922). Life of the Cyclones and the Polar Front Theory
438 of Atmospheric Circulation. *Geophysisks Publikationer*, *3*(1), 18.
- 439 Cao, Y., Li, C., & Dong, C. (2020). Atmospheric Cold Front-Generated Waves in
440 the Coastal Louisiana. *Journal of Marine Science and Engineering*, *8*(11), 900.
441 doi: 10.3390/jmse8110900
- 442 Catto, J. L., & Pfahl, S. (2013). The importance of fronts for extreme precipita-
443 tion. *Journal of Geophysical Research: Atmospheres*, *118*(19), 10,791–10,801.
444 doi: 10.1002/jgrd.50852
- 445 Chen, F., & Dudhia, J. (2001). Coupling an Advanced Land Surface–Hydrology
446 Model with the Penn State–NCAR MM5 Modeling System. Part I: Model Im-
447 plementation and Sensitivity. *Monthly Weather Review*, *129*(4), 569–585. doi:
448 10.1175/1520-0493(2001)129<0569:CAALSH>2.0.CO;2
- 449 Chen, G., Chapron, B., Ezraty, R., & Vandemark, D. (2002). A Global View of
450 Swell and Wind Sea Climate in the Ocean by Satellite Altimeter and Scat-
451 terometer. *Journal of Atmospheric and Oceanic Technology*, *19*(11), 1849–
452 1859. doi: 10.1175/1520-0426(2002)019<1849:AGVOSA>2.0.CO;2
- 453 Chen, S. S., & Curcic, M. (2016). Ocean surface waves in Hurricane Ike (2008) and
454 Superstorm Sandy (2012): Coupled model predictions and observations. *Ocean*

- 455 *Modelling*, 103, 161–176. doi: 10.1016/j.ocemod.2015.08.005
- 456 Chen, S. S., Zhao, W., Donelan, M. A., & Tolman, H. L. (2013). Directional
457 Wind–Wave Coupling in Fully Coupled Atmosphere–Wave–Ocean Models:
458 Results from CBLAST-Hurricane. *Journal of the Atmospheric Sciences*,
459 70(10), 3198–3215. doi: 10.1175/JAS-D-12-0157.1
- 460 Chen, X., Ginis, I., & Hara, T. (2020). Impact of Shoaling Ocean Surface Waves
461 on Wind Stress and Drag Coefficient in Coastal Waters: 2. Tropical Cy-
462 clones. *Journal of Geophysical Research: Oceans*, 125(7), e2020JC016223.
463 doi: 10.1029/2020JC016223
- 464 Edson, J. B., Jampana, V., Weller, R. A., Bigorre, S. P., Plueddemann, A. J.,
465 Fairall, C. W., ... Hersbach, H. (2013). On the Exchange of Momentum
466 over the Open Ocean. *Journal of Physical Oceanography*, 43(8), 1589–1610.
467 doi: 10.1175/JPO-D-12-0173.1
- 468 Egbert, G. D., & Erofeeva, S. Y. (2002). Efficient Inverse Modeling of Barotropic
469 Ocean Tides. *Journal of Atmospheric and Oceanic Technology*, 19(2), 183–204.
470 doi: 10.1175/1520-0426(2002)019<0183:EIMOBO>2.0.CO;2
- 471 Fairall, C. W., Bradley, E. F., Hare, J. E., Grachev, A. A., & Edson, J. B.
472 (2003). Bulk Parameterization of Air–Sea Fluxes: Updates and Verifica-
473 tion for the COARE Algorithm. *Journal of Climate*, 16(4), 571–591. doi:
474 10.1175/1520-0442(2003)016<0571:BPOASF>2.0.CO;2
- 475 Fairall, C. W., Bradley, E. F., Rogers, D. P., Edson, J. B., & Young, G. S. (1996).
476 Bulk parameterization of air-sea fluxes for Tropical Ocean–Global Atmosphere
477 Coupled–Ocean Atmosphere Response Experiment. *Journal of Geophysical*
478 *Research: Oceans*, 101(C2), 3747–3764. doi: 10.1029/95JC03205
- 479 Grachev, A. A., & Fairall, C. W. (2001). Upward Momentum Transfer in the Marine
480 Boundary Layer. *Journal of Physical Oceanography*, 31(7), 1698–1711. doi: 10
481 .1175/1520-0485(2001)031<1698:UMTITM>2.0.CO;2
- 482 Guo, B., Subrahmanyam, M. V., & Li, C. (2020). Waves on Louisiana Continental
483 Shelf Influenced by Atmospheric Fronts. *Scientific Reports*, 10(1), 272. doi: 10
484 .1038/s41598-019-55578-w
- 485 Haidvogel, D. B., Arango, H. G., Hedstrom, K., Beckmann, A., Malanotte-
486 Rizzoli, P., & Shechetkin, A. F. (2000). Model evaluation experiments
487 in the North Atlantic Basin: Simulations in nonlinear terrain-following co-

- 488 ordinates. *Dynamics of Atmospheres and Oceans*, 32(3), 239–281. doi:
 489 10.1016/S0377-0265(00)00049-X
- 490 Hanley, K. E., & Belcher, S. E. (2008). Wave-Driven Wind Jets in the Marine At-
 491 mospheric Boundary Layer. *Journal of the Atmospheric Sciences*, 65(8), 2646–
 492 2660. doi: 10.1175/2007JAS2562.1
- 493 Hanley, K. E., Belcher, S. E., & Sullivan, P. P. (2010). A Global Climatology of
 494 Wind-Wave Interaction. *Journal of Physical Oceanography*, 40(6), 1263–1282.
 495 doi: 10.1175/2010JPO4377.1
- 496 Hasselmann, S., Hasselmann, K., Allender, J. H., & Barnett, T. P. (1985). Compu-
 497 tations and Parameterizations of the Nonlinear Energy Transfer in a Gravity-
 498 Wave Spectrum. Part II: Parameterizations of the Nonlinear Energy Transfer
 499 for Application in Wave Models. *Journal of Physical Oceanography*, 15(11),
 500 1378–1391. doi: 10.1175/1520-0485(1985)015<1378:CAPOTN>2.0.CO;2
- 501 Hersbach, H., Bell, B., Berrisford, P., Hirahara, S., Horányi, A., Muñoz-Sabater, J.,
 502 ... Thépaut, J.-N. (2020). The ERA5 global reanalysis. *Quarterly Journal of*
 503 *the Royal Meteorological Society*, 146(730), 1999–2049. doi: 10.1002/qj.3803
- 504 Hewson, T. D. (1998). Objective fronts. *Meteorological Applications*, 5(1), 37–65.
 505 doi: 10.1017/S1350482798000553
- 506 Hong, S.-Y., & Lim, J.-O. J. (2006). The WRF Single-Moment 6-Class Microphysics
 507 Scheme (WSM6). *JOURNAL OF THE KOREAN METEOROLOGICAL SO-*
 508 *CIETY*.
- 509 Hsu, J.-Y., Lien, R.-C., D’Asaro, E. A., & Sanford, T. B. (2019). Scaling of Drag
 510 Coefficients Under Five Tropical Cyclones. *Geophysical Research Letters*,
 511 46(6), 3349–3358. doi: 10.1029/2018GL081574
- 512 Iacono, M. J., Delamere, J. S., Mlawer, E. J., Shephard, M. W., Clough, S. A., &
 513 Collins, W. D. (2008). Radiative forcing by long-lived greenhouse gases: Cal-
 514 culations with the AER radiative transfer models. *Journal of Geophysical*
 515 *Research: Atmospheres*, 113(D13). doi: 10.1029/2008JD009944
- 516 Jiménez, P. A., Dudhia, J., González-Rouco, J. F., Navarro, J., Montávez, J. P.,
 517 & García-Bustamante, E. (2012). A Revised Scheme for the WRF Sur-
 518 face Layer Formulation. *Monthly Weather Review*, 140(3), 898–918. doi:
 519 10.1175/MWR-D-11-00056.1
- 520 Kim, J.-Y., Kaihatu, J., Chang, K.-A., Sun, S.-H., Huff, T. P., & Feagin, R. A.

- 521 (2020). Effect of Cold Front-Induced Waves Along Wetlands Boundaries.
 522 *Journal of Geophysical Research: Oceans*, *125*(12), e2020JC016603. doi:
 523 10.1029/2020JC016603
- 524 Kukulka, T., & Hara, T. (2005). Momentum flux budget analysis of wind-driven air-
 525 water interfaces. *Journal of Geophysical Research: Oceans*, *110*(C12). doi: 10
 526 .1029/2004JC002844
- 527 Large, W. G., McWilliams, J. C., & Doney, S. C. (1994). Oceanic vertical mixing: A
 528 review and a model with a nonlocal boundary layer parameterization. *Reviews*
 529 *of Geophysics*, *32*(4), 363–403. doi: 10.1029/94RG01872
- 530 Lellouche, J.-M., Greiner, E., Le Galloudec, O., Garric, G., Regnier, C., Drevillon,
 531 M., ... Le Traon, P.-Y. (2018). Recent updates to the Copernicus Marine
 532 Service global ocean monitoring and forecasting real-time 1/12° high-resolution
 533 system. *Ocean Science*, *14*(5), 1093–1126. doi: 10.5194/os-14-1093-2018
- 534 Liu, Q., Rogers, W. E., Babanin, A. V., Young, I. R., Romero, L., Zieger, S., ...
 535 Guan, C. (2019). Observation-Based Source Terms in the Third-Generation
 536 Wave Model WAVEWATCH III: Updates and Verification. *Journal of Physical*
 537 *Oceanography*, *49*(2), 489–517. doi: 10.1175/JPO-D-18-0137.1
- 538 Makin, V. K., Kudryavtsev, V. N., & Mastenbroek, C. (1995). Drag of the sea sur-
 539 face. *Boundary-Layer Meteorology*, *73*(1), 159–182. doi: 10.1007/BF00708935
- 540 Nakanishi, M., & Niino, H. (2009). Development of an Improved Turbulence Closure
 541 Model for the Atmospheric Boundary Layer. *Journal of the Meteorological So-*
 542 *ciety of Japan. Ser. II*, *87*(5), 895–912. doi: 10.2151/jmsj.87.895
- 543 Olson, J. B., Smirnova, T., Kenyon, J. S., Turner, D. D., Brown, J. M., Zheng, W.,
 544 & Green, B. W. (2021). A Description of the MYNN Surface-Layer Scheme.
 545 *NOAA Technical Memorandum OAR GSL*. doi: 10.25923/F6A8-BC75
- 546 Parfitt, R., Czaja, A., Minobe, S., & Kuwano-Yoshida, A. (2016). The atmospheric
 547 frontal response to SST perturbations in the Gulf Stream region. *Geophysical*
 548 *Research Letters*, *43*(5), 2299–2306. doi: 10.1002/2016GL067723
- 549 Parfitt, R., Czaja, A., & Seo, H. (2017). A simple diagnostic for the detection of
 550 atmospheric fronts. *Geophysical Research Letters*, *44*(9), 4351–4358. doi: 10
 551 .1002/2017GL073662
- 552 Phillips, O. M. (1966). *The Dynamics of the Upper Ocean*. Cambridge U.P.
- 553 Porchetta, S., Temel, O., Muñoz-Esparza, D., Reuder, J., Monbaliu, J., Van Beeck,

- 554 J., & Van Lipzig, N. (2019). A new roughness length parameterization ac-
 555 counting for wind–wave (mis)alignment. *Atmospheric Chemistry and Physics*,
 556 *19*(10), 6681–6700. doi: 10.5194/acp-19-6681-2019
- 557 Porchetta, S., Temel, O., Warner, J., Muñoz-Esparza, D., Monbaliu, J., Van Beeck,
 558 J., & Van Lipzig, N. (2021). Evaluation of a roughness length parametrization
 559 accounting for wind–wave alignment in a coupled atmosphere–wave model.
 560 *Quarterly Journal of the Royal Meteorological Society*, *147*(735), 825–846. doi:
 561 10.1002/qj.3948
- 562 Rasclé, N., & Ardhuin, F. (2013). A global wave parameter database for geophysical
 563 applications. Part 2: Model validation with improved source term parameteri-
 564 zation. *Ocean Modelling*, *70*, 174–188. doi: 10.1016/j.ocemod.2012.12.001
- 565 Reeder, M. J., Spengler, T., & Spensberger, C. (2021). The Effect of Sea Surface
 566 Temperature Fronts on Atmospheric Frontogenesis. *Journal of the Atmospheric*
 567 *Sciences*, *78*(6), 1753–1771. doi: 10.1175/JAS-D-20-0118.1
- 568 Reichl, B. G., Hara, T., & Ginis, I. (2014). Sea state dependence of the wind
 569 stress over the ocean under hurricane winds. *Journal of Geophysical Research:*
 570 *Oceans*, *119*(1), 30–51. doi: 10.1002/2013JC009289
- 571 Sauvage, C., Seo, H., Clayson, C. A., & Edson, J. B. (2023). Improving Wave-Based
 572 Air–Sea Momentum Flux Parameterization in Mixed Seas. *Journal of Geophys-*
 573 *ical Research: Oceans*, *128*(3), e2022JC019277. doi: 10.1029/2022JC019277
- 574 Seo, H., Miller, A. J., & Norris, J. R. (2016). Eddy–Wind Interaction in the Cali-
 575 fornia Current System: Dynamics and Impacts. *Journal of Physical Oceanogra-*
 576 *phy*, *46*(2), 439–459. doi: 10.1175/JPO-D-15-0086.1
- 577 Seo, H., Miller, A. J., & Roads, J. O. (2007). The Scripps Coupled
 578 Ocean–Atmosphere Regional (SCOAR) Model, with Applications in the
 579 Eastern Pacific Sector. *Journal of Climate*, *20*(3), 381–402. doi: 10.1175/
 580 JCLI4016.1
- 581 Seo, H., O’Neill, L. W., Bourassa, M. A., Czaja, A., Drushka, K., Edson, J. B., ...
 582 Wang, Q. (2023). Ocean Mesoscale and Frontal-Scale Ocean–Atmosphere
 583 Interactions and Influence on Large-Scale Climate: A Review. *Journal of*
 584 *Climate*, *36*(7), 1981–2013. doi: 10.1175/JCLI-D-21-0982.1
- 585 Seo, H., Song, H., O’Neill, L. W., Mazloff, M. R., & Cornuelle, B. D. (2021).
 586 Impacts of ocean currents on the South Indian Ocean extratropical storm

- 587 track through the relative wind effect. *Journal of Climate*, 1–61. doi:
588 10.1175/JCLI-D-21-0142.1
- 589 Seo, H., Subramanian, A. C., Miller, A. J., & Cavanaugh, N. R. (2014). Cou-
590 pled Impacts of the Diurnal Cycle of Sea Surface Temperature on the Mad-
591 den–Julian Oscillation. *Journal of Climate*, 27(22), 8422–8443. doi:
592 10.1175/JCLI-D-14-00141.1
- 593 Shchepetkin, A. F., & McWilliams, J. C. (2005). The regional oceanic model-
594 ing system (ROMS): A split-explicit, free-surface, topography-following-
595 coordinate oceanic model. *Ocean Modelling*, 9(4), 347–404. doi: 10.1016/
596 j.ocemod.2004.08.002
- 597 Shin, H. H., Hong, S.-Y., & Dudhia, J. (2012). Impacts of the Lowest Model Level
598 Height on the Performance of Planetary Boundary Layer Parameterizations.
599 *Monthly Weather Review*, 140(2), 664–682. doi: 10.1175/MWR-D-11-00027.1
- 600 Skamarock, C., Klemp, B., Dudhia, J., Gill, O., Liu, Z., Berner, J., . . . Huang, X.-y.
601 (2019). A Description of the Advanced Research WRF Model Version 4.1. (*No.*
602 *NCAR/TN-556+STR*). doi: 10.5065/1dfh-6p97
- 603 Soster, F., & Parfitt, R. (2022). On Objective Identification of Atmospheric Fronts
604 and Frontal Precipitation in Reanalysis Datasets. *Journal of Climate*, 35(14),
605 4513–4534. doi: 10.1175/JCLI-D-21-0596.1
- 606 Steffen, J., Seo, H., Clayson, C. A., Pei, S., & Shinoda, T. (2023). Impacts of tidal
607 mixing on diurnal and intraseasonal air-sea interactions in the Maritime Con-
608 tinent. *Deep Sea Research Part II: Topical Studies in Oceanography*, 212,
609 105343. doi: 10.1016/j.dsr2.2023.105343
- 610 Stopa, J. E., Ardhuin, F., Babanin, A., & Zieger, S. (2016). Comparison and valida-
611 tion of physical wave parameterizations in spectral wave models. *Ocean Mod-*
612 *elling*, 103, 2–17. doi: 10.1016/j.ocemod.2015.09.003
- 613 Sullivan, P. P., Edson, J. B., Hristov, T., & McWilliams, J. C. (2008). Large-Eddy
614 Simulations and Observations of Atmospheric Marine Boundary Layers above
615 Nonequilibrium Surface Waves. *Journal of the Atmospheric Sciences*, 65(4),
616 1225–1245. doi: 10.1175/2007JAS2427.1
- 617 The WAVEWATCH III Development Group, W. (2019). *User manual and system*
618 *documentation of WAVEWATCH III R© version 6.07* (Tech. Note 333). Col-
619 lege Park, MD, USA,: NOAA/NWS/NCEP/MMAB,.

- 620 Tolman, H. L., Balasubramanian, B., Burroughs, L. D., Chalikov, D. V., Chao,
621 Y. Y., Chen, H. S., & Gerald, V. M. (2002). Development and Implemen-
622 tation of Wind-Generated Ocean Surface Wave Models at NCEP. *Weather
623 and Forecasting*, *17*(2), 311–333. doi: 10.1175/1520-0434(2002)017<0311:
624 DAIOWG>2.0.CO;2
- 625 Trowbridge, J., Weller, R., Kelley, D., Dever, E., Plueddemann, A., Barth, J. A., &
626 Kawka, O. (2019). The Ocean Observatories Initiative. *Frontiers in Marine
627 Science*, *6*.
- 628 Zheng, Y., Alapaty, K., Herwehe, J. A., Genio, A. D. D., & Niyogi, D. (2016). Im-
629 proving High-Resolution Weather Forecasts Using the Weather Research and
630 Forecasting (WRF) Model with an Updated Kain–Fritsch Scheme. *Monthly
631 Weather Review*, *144*(3), 833–860. doi: 10.1175/MWR-D-15-0005.1
- 632 Zhou, X., Hara, T., Ginis, I., D’Asaro, E., Hsu, J.-Y., & Reichl, B. G. (2022). Drag
633 Coefficient and Its Sea State Dependence under Tropical Cyclones. *Journal of
634 Physical Oceanography*, *52*(7), 1447–1470. doi: 10.1175/JPO-D-21-0246.1

Misaligned Wind-Waves Behind Atmospheric Cold Fronts

César Sauvage¹, Hyodae Seo¹, Benjamin W. Barr¹, James B. Edson¹, and Carol Anne Clayson¹.

¹Woods Hole Oceanographic Institution, Woods Hole, Massachusetts, USA

Key Points:

- Passing atmospheric cold fronts generate a large area of growing wind-waves that are misaligned with local wind.
- The misaligned waves increase the roughness length, drag and enthalpy exchange coefficients, and wind stress.
- Representation of the misaligned wave effect in the bulk formula improves the momentum flux estimates.

Corresponding author: César Sauvage, csauvage@whoi.edu

Abstract

13
14 Atmospheric fronts embedded in extratropical cyclones are high-impact weather phenom-
15 ena, contributing significantly to midlatitude winter precipitation. The three vital char-
16 acteristics of the atmospheric fronts, high wind speeds, abrupt change in wind direction,
17 and rapid translation, force the induced surface waves to be misaligned with winds ex-
18 clusively behind the cold fronts. The effects of the misaligned waves on air-sea fluxes re-
19 main undocumented. Using the multi-year in situ near-surface observations and direct
20 covariance flux measurements from the Pioneer Array off the coast of New England, we
21 find that the majority of the passing cold fronts generate misaligned waves behind the
22 cold front. Once generated, the waves remain misaligned, on average, for about 8 hours.
23 The fully-coupled model simulations indicate that the misaligned waves significantly in-
24 crease the roughness length (300%), drag coefficient (30%), and momentum flux (20%).
25 The increased surface drag reduces the wind speeds in the surface layer. The upward tur-
26 bulent heat flux is weakly decreased by the misaligned waves because of the compensat-
27 ing effect between the decrease in temperature and humidity scaling parameters and the
28 increase in friction velocity. The misaligned wave effect is not accurately represented in
29 a commonly used wave-based bulk flux algorithm. Yet, the suggested modification to the
30 current formulation improves the overall accuracy of parameterized momentum flux es-
31 timates. The results imply that better representing a directional wind-wave coupling in
32 the bulk formula of the numerical models may help improve the air-sea interaction sim-
33 ulations under the passing atmospheric fronts in the midlatitudes.

Plain Language Summary

34
35 Atmospheric fronts are recurrent weather phenomena in midlatitudes, significantly
36 contributing to winter precipitation. They are characterized by high wind speeds, abrupt
37 change in wind direction, and rapid translation. Their passage over the ocean lead to
38 the generation of strongly misaligned waves, particularly behind the cold fronts. The ef-
39 fects of these misaligned waves on air-sea fluxes remain undocumented. Using the long
40 term surface observations from the Pioneer Array off the coast of New England, we find
41 that the majority of the passing atmospheric fronts generate misaligned waves behind
42 the cold front which can remain misaligned, on average, for about 8 hours. The use of
43 coupled numerical experiments indicate that the misaligned waves significantly increase
44 the ocean roughness length and momentum flux, which reduce the surface wind speeds.

45 The misaligned wave effect is not accurately represented in a commonly used wave based
46 air-sea flux algorithm. Yet, the suggested modification to the current formulation im-
47 proves the overall accuracy of parameterized momentum flux estimates. The results im-
48 ply that better representing a directional wind-wave coupling in numerical models may
49 help improve the air-sea interaction simulations under the passing atmospheric fronts
50 in the midlatitudes.

51 **1 Introduction**

52 Air-sea momentum, heat, and moisture exchanges are mediated by interactions be-
53 tween near-surface atmospheric turbulence and the ocean surface wave field. Wave fields
54 are complex and may include contributions from a wide range of frequencies and direc-
55 tions, including strongly coupled short wind-waves with wavelengths of $O(0.1-10\text{ m})$ and
56 frequencies higher than twice the spectral peak (Phillips, 1966; Makin et al., 1995; Kukulka
57 & Hara, 2005), developing to mature locally generated wind-waves and remotely gen-
58 erated long-period swell. In many current modern sea state-dependent (or wave-based)
59 bulk flux algorithms, the surface waves that determine the surface drag are often assumed
60 to be in the direction of winds. However, there are many wind and wave regimes where
61 this assumption is not valid and where using it can yield notable deficiencies in the pa-
62 rameterized momentum flux. Swell waves under the low-wind condition (Grachev & Fairall,
63 2001; G. Chen et al., 2002; Hanley & Belcher, 2008; Hanley et al., 2010; Sullivan et al.,
64 2008) or the mixed seas under the trade wind (Sauvage et al., 2023) or tropical cyclones
65 (S. S. Chen et al., 2013; Reichl et al., 2014; S. S. Chen & Curcic, 2016; Hsu et al., 2019;
66 X. Chen et al., 2020) are well-known examples in the lower-latitudes. Existing studies
67 suggest a complex relationship between wind-wave misalignment and surface stress, which
68 may be regime-dependent (e.g., high winds in tropical cyclones vs. lower winds in mid-
69 latitudes). For instance, Zhou et al. (2022) found that misalignment between local winds
70 and tropical cyclone-generated swell reduced the drag coefficient in high winds, suggest-
71 ing quadrant-specific variations in drag due to storm-scale misalignment patterns. On
72 the other hand, Porchetta et al. (2019) examined in situ observations from the North Sea
73 and the U.S. New England coast and found that wind-wave misalignment increases the
74 surface drag, with additional influence by wave age.

75 In the midlatitudes, the atmospheric fronts are embedded in the extratropical cy-
76 clones and significantly modulate the day-to-day weather variability. They feature elon-

77 gated along-frontal scales of 1000s km comparable to the lateral extent of the extratrop-
78 ical cyclones, but much shorter cross-frontal scales of 10-100 km (Figure 1, Bjerknes &
79 Solberg, 1922). Figure 1a shows a typical extratropical cyclone we will examine in this
80 study. Traveling rapidly eastward at ≈ 10 m/s, the atmospheric fronts accompany gale-
81 force near-surface winds (15-30 m/s), which also abruptly shift in direction from the southerly
82 in the warm sector to the northwesterly in the cold sector. Although atmospheric fronts
83 typically occur 10-30% in the wintertime North Atlantic (Hewson, 1998; Berry et al., 2011;
84 Parfitt et al., 2017; Reeder et al., 2021), they are known to contribute to up to 90% of
85 the precipitation (Catto & Pfahl, 2013; Soster & Parfitt, 2022), often in an extreme form
86 (Catto & Pfahl, 2013) and, hence, they are one of the most important high-impact weather
87 phenomena in the midlatitudes. Interactions between the cold airmass of the fronts and
88 the warmer ocean (and ocean fronts) via air-sea turbulent heat fluxes influence the in-
89 tensity of these events (Parfitt et al., 2016; Seo et al., 2023). The atmospheric cold fronts
90 are also known to force significant surges and complex wave reactions that severely im-
91 pact coastal and estuary circulations and wetland evolutions (Kim et al., 2020; Cao et
92 al., 2020; Guo et al., 2020). However, their impacts on surface drag and momentum flux
93 in the midlatitudes are undocumented in the literature. We will demonstrate that di-
94 rectional wave-wind coupling can modulate these surface fluxes, impacting the surface
95 drag and near-surface winds.

96 The three crucial characteristics of the atmospheric fronts relevant to misaligned
97 waves are high winds, abrupt changes in wind direction, and rapid translation. In the
98 warm sector of the fronts, the strong southerly winds force the strongly coupled short
99 wind-waves, generally aligned with the winds. Once the cold front is crossed, the marked
100 shift in the wind direction, combined with the rapid eastward translation, generates a
101 large fetch of growing wind-waves that become quickly misaligned with the northwest-
102 erly winds. Figure 1b illustrates this process schematically. Here, we define that the waves
103 are misaligned with winds when the propagation direction of the most dominant wave
104 differs from the wind direction by $>60^\circ$. Not only is this definition intuitive, but it is
105 also consistent with the observed changes in directional wave spreading across the cold
106 front (not shown).

107 This study identifies and examines the evolutions of misaligned waves under atmo-
108 spheric fronts using direct in-situ surface flux measurements and fully-coupled high-resolution
109 ocean-atmosphere-wave model simulations. A possible modification to more accurately

110 represent the relevant wave-wind physics in the bulk flux parameterization is also dis-
111 cussed. Section 2 describes the observations, parameterizations, and model simulations.
112 Section 3 provides a case study investigation of misaligned waves for one atmospheric
113 front case using model simulations and observations, while Section 4 offers the climato-
114 logical perspectives of the evolution of misaligned waves and their impacts on param-
115 eterized flux using observations. Section 5 concludes the study.

116 **2 Methods**

117 **2.1 Observations**

118 The Pioneer Array, located off the coast of New England and operated by the NSF
119 Ocean Observatories Initiative (OOI, Trowbridge et al., 2019), provides various mete-
120 orological and ocean observations of physical, chemical, and biological processes from De-
121 cember 2014 until November 2022. This study uses the 8-years of near-surface measure-
122 ments of wind, temperature, humidity, and surface wave fields. We also use the momen-
123 tum fluxes from the direct covariance flux system (DCFS), available over a shorter pe-
124 riod (2015-05-13 - 2015-10-23; 2016-05-13 - 2018-03-29; 2018-10-30 - 2019-04-07). NOAA’s
125 National Data Buoy Center (NDBC) buoys off the New England coast are also used, es-
126 pecially surface wave information, including 2D wave spectrum along with significant wave
127 height, dominant wave period, and mean/peak wave direction, co-located with the near-
128 surface measurements of winds, temperature, humidity, pressure, and ocean surface tem-
129 perature.

130 **2.2 SCOAR coupled regional modeling system**

131 We use the Scripps Coupled Ocean-Atmosphere Regional model (SCOAR, Seo et
132 al., 2007, 2014, 2016, 2021; Sauvage et al., 2023), which couples the Weather Research
133 and Forecast model (WRF, Skamarock et al., 2019) in the atmosphere to the Regional
134 Ocean Modeling System (ROMS, Haidvogel et al., 2000; Shchepetkin & McWilliams, 2005)
135 in the ocean and WAVEWATCH III (WW3, Tolman et al., 2002; The WAVEWATCH
136 III Development Group, 2019) for the surface waves. ROMS is driven by the momen-
137 tum, heat, and freshwater fluxes parameterized from COARE3.5 (Fairall et al., 1996, 2003;
138 Edson et al., 2013) implemented in the WRF Mellor-Yamada-Nakanishi-Niino (MYNN)
139 surface layer scheme (Nakanishi & Niino, 2009; Jiménez et al., 2012). ROMS forces WRF

140 by feeding SST and surface current vectors to the WRF surface layer scheme. Between
 141 WRF and WW3, the model offers various wave-to-atmosphere coupling options to de-
 142 termine the surface fluxes, as documented in detail in Sauvage et al. (2023). This study
 143 will examine two particular wave-based roughness length formulations, as described in
 144 Section 2.3. ROMS provides surface current to WW3 to represent the current effect on
 145 waves. WW3 can also be coupled to ROMS to represent energy dissipation due to wave-
 146 breaking and whitecapping. However, the WW3-ROMS coupling is not considered in this
 147 study.

148 2.3 Momentum flux parameterizations

149 The momentum flux (τ), sensible (H_s) and latent (H_l) heat fluxes are parameter-
 150 ized via COARE (Fairall et al., 1996) as:

$$\tau = \rho_a C_D S_r U_r = \rho_a u_*^2, \quad (1)$$

$$H_s = \rho_a C_{pa} C_h S_r \Delta T = -\rho_a C_{pa} u_* T_*, \quad (2)$$

$$H_l = \rho_a L_e C_e S_r \Delta Q = -\rho_a L_e u_* q_*, \quad (3)$$

151 where ρ_a is the air density, C_{pa} is the specific heat capacity of the air at constant
 152 pressure, L_e is the latent heat of evaporation, T is the potential temperature, Q is the
 153 water vapor mixing ratio, S_r is the scalar averaged wind speed relative to the ocean sur-
 154 face, U_r is the magnitude of the wind vector relative to the ocean surface, C_D , C_h , C_e
 155 are the transfer coefficients for stress, sensible and latent heat, and u_* , T_* , q_* are the Monin-
 156 Obukhov similarity scaling parameters. The drag coefficient C_D is defined as:

$$C_D(z, z_0, \psi_m) = \left[\frac{\kappa}{\ln(z/z_0) - \psi_m(\zeta)} \right]^2, \quad (4)$$

157 where κ is the von Kármán constant, $\psi_m(\zeta)$ is an empirical function of atmospheric
 158 stability, ζ is the z/L ratio with L the Obukhov length and z the height above the sur-
 159 face. The COARE wave-based formulation (Edson et al., 2013) parameterizes the wave-
 160 induced surface roughness (z_0^{rough} , hereafter simply z_0) as,

$$z_0 = H_s D \left(\frac{u_*}{c_p} \right)^B, \quad (5)$$

161 where H_s is the significant wave height, u_*/c_p is the inverse wave age based on u_* , and
 162 the peak phase speed of the wave (c_p). D and B are numerical constants given by $D =$

163 0.09 and $B = 2$ (Edson et al., 2013). In addition to Eq. 5 included in the COARE3.5
 164 public release, Sauvage et al. (2023) tested a revised formulation, in which z_0 increases
 165 as the wave-wind misalignment increases (Porchetta et al., 2019, 2021),

$$z_0 = H_s D \cos(a\theta) \left(\frac{u_*}{c_p}\right)^{B \cos(b\theta)}, \quad (6)$$

166 where θ is the absolute directional difference between the 10-m wind and the peak wave
 167 direction. D and B are the same coefficients as in Eq. 5, while the coefficients $a = 0.45$
 168 and $b = -0.32$ are determined by Porchetta et al. (2019) from a set of midlatitude off-
 169 shore in situ measurements, including the Air-Sea Interaction Tower (ASIT) south of Martha’s
 170 Vineyard, which is close to the region of the current study.

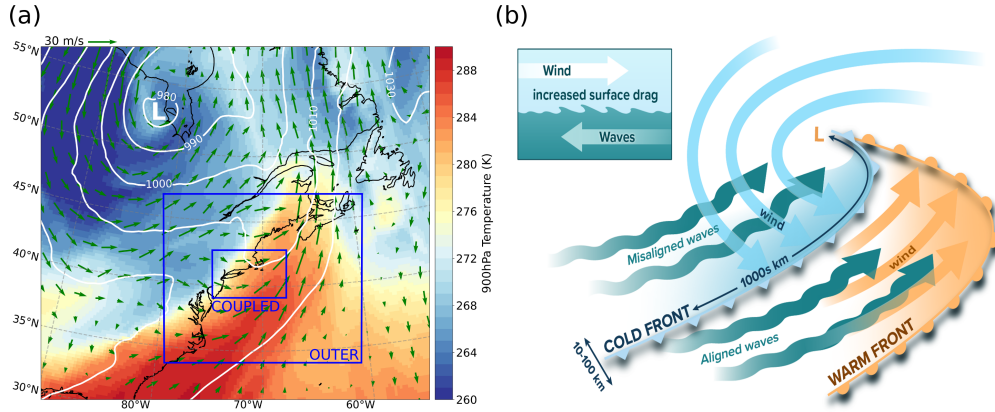


Figure 1. (a) An extratropical cyclone in the North Atlantic on December 6, 2017, at 12:00 UTC, showing the potential temperature at 900 hPa (K), overlaid with the mean sea level pressure (contours, hPa) and the 900 hPa wind (arrows), from the ERA5 reanalysis. The extent of the outer and nested model domains is also indicated. (b) A schematic representation of an atmospheric front passing over the ocean showing aligned wind-waves under the warm sector and strongly misaligned waves behind the cold front. The schematic at the top left represents the mechanism of the enhanced drag behind the cold front when wind and waves are misaligned. The "L" symbol denotes the center of the low-pressure system in both (a,b).

171 2.4 Experiments

172 The model domain covers the North Atlantic (Figure 1a) with a nested configura-
 173 tion. In the outer domain, the model is run at 7.5 km resolution and is atmosphere-
 174 only, dynamically downscaling the large-scale atmospheric circulation with spectral nudg-

175 ing. This drives the inner domain zooming over the US Northeast (Figure 1a), where WRF,
 176 ROMS, and WW3 are fully coupled at an hourly frequency and run at the identical 1.5
 177 km resolution with matching grids and land-sea masks. ROMS has 30 vertical levels with
 178 a stretched vertical grid that enables the enhanced resolutions near the surface and the
 179 bottom, with $\theta_s = 7.0$, $\theta_b = 0.1$, and $h_{cline} = 300$ m, yielding a minimum of 15 layers in
 180 the upper 150 m. The vertical resolution of WRF is refined to have 50 vertical levels with
 181 ≈ 20 levels below 250 m. The lowest level is close to the surface (5.5 m), with the 2nd
 182 lowest level at 12 m per Shin et al. (2012).

183 In WRF, deep cumulus convection is represented through the Multi-scale Kain-Fritsch
 184 scheme (Zheng et al., 2016), the cloud micro-physics by the WRF single-moment 6-class
 185 scheme (Hong & Lim, 2006), the land surface process by the Noah land surface model
 186 (F. Chen & Dudhia, 2001), and the Rapid Radiative Transfer Model for general circu-
 187 lation models (RRTMG, Iacono et al., 2008) for the shortwave and longwave radiations.
 188 The planetary boundary layer (PBL) processes are treated with the MYNN level 2.5 scheme
 189 (Nakanishi & Niino, 2009). In ROMS, the KPP (K profile parameterization) scheme (Large
 190 et al., 1994) determines vertical eddy viscosity and diffusivity. In WW3, the ST6 pack-
 191 age is used to parameterize wind input, wave breaking, and swell dissipation (Babanin,
 192 2011; Stopa et al., 2016; Liu et al., 2019). Nonlinear wave-wave interactions are com-
 193 puted using the discrete interaction approximation (Hasselmann et al., 1985). Reflec-
 194 tion by shorelines is enabled through the Arduin and Roland (2012) scheme. The depth-
 195 induced breaking is based on Battjes and Janssen (1978), and the bottom friction for-
 196 mulation follows Arduin et al. (2003).

197 Two coupled model simulations are run for a 3-day case study (December 5-8, 2017)
 198 featuring one passing atmospheric front (Figure 1a). In the simulation dubbed *WBF θ* ,
 199 the roughness length is parameterized by Eq. 6, where the wind and wave misalignment
 200 effect is considered. This will be compared to another simulation, called *WBF*, where
 201 such an effect is omitted (Eq. 5). In both simulations, the WRF model is initialized and
 202 driven by the 1-hr 0.25° ERA5 reanalysis (Hersbach et al., 2020), ROMS by the daily
 203 1/12° MERCATOR International global reanalysis (Lellouche et al., 2018), and WW3
 204 by 11 spectral points obtained from the global 1/2° WW3 simulations (Rascle & Ar-
 205 duin, 2013). The initial conditions for WW3 were obtained from the 30-day spin-up sim-
 206 ulations forced by ERA5 atmospheric forcing. In ROMS, the tidal forcing is obtained
 207 using the Oregon State University Tidal Prediction Software (Egbert & Erofeeva, 2002)

208 and applied as a 2-D open boundary condition by prescribing the tidal period, elevation
 209 amplitude, current phase angle, current inclination angle, the minimum, and maximum
 210 tidal current, and ellipse semi-minor axes for 13 major tidal constituents (Steffen et al.,
 211 2023).

212 3 Case Study Examination

213 This section uses in situ observations and model simulations to examine the mis-
 214 aligned waves during one atmospheric front. To provide spatial context, we will discuss
 215 the model results first. Figure 2 compares three stages of a cold front passage, showing
 216 the directional misalignment (θ) and the wind-speed-based wave age ($\chi = c_p/U_{10}$) for
 217 three different times: December 6 at 09:00 UTC, when the Pioneer Array is ahead of the
 218 cold front (pre-cold-front), at 12:00 UTC (cold-front), and at 15:00 UTC (post-cold-front).
 219 Hereafter, U_{10} is defined as $U_{10} = (U_{10x}^2 + U_{10y}^2)^{1/2}$ where U_{10x} is the zonal and U_{10y}
 220 is the meridional wind components.

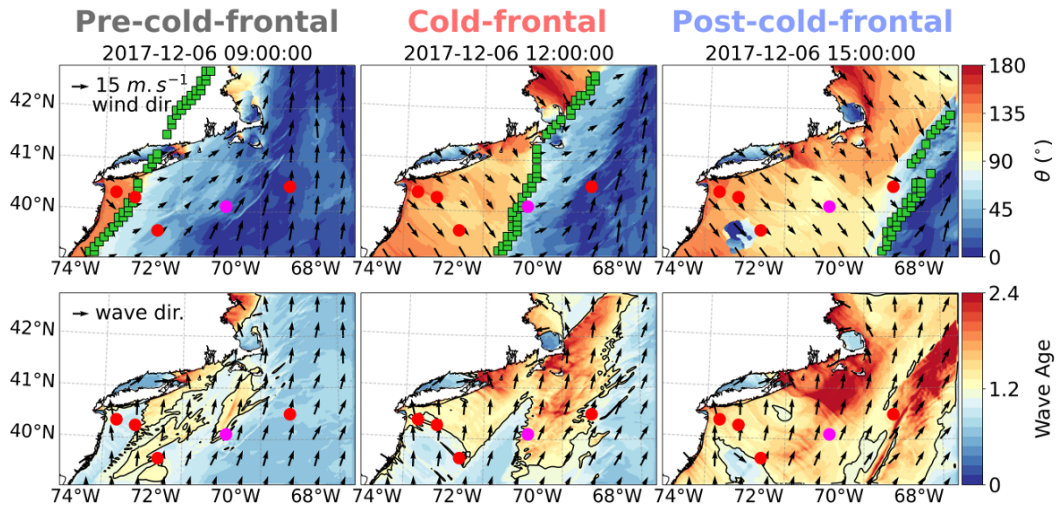


Figure 2. The top row shows the evolution of θ (shading), overlaid with the surface wind (black arrows) as simulated from the WBF θ run at 09:00 (pre-cold-front), 12:00 (cold-front) and 15:00 (post-cold-front) UTC on December 6, 2017. The green markers indicate the detected cold front using the Parfitt et al. (2017) algorithm. The bottom row shows the evolution of the wave age, overlaid with the wave peak direction (normalized black arrows). A wave age of 1.2 is indicated by a black contour. The magenta circle denotes the location of the Pioneer Array, and the 4 red circles are the NDBC moorings (from left to right: mooring identification numbers 44065, 44025, 44066, and 44008).

221 3.1 Evolutions of winds and waves

222 During the pre-cold-front, the directional misalignment is generally small ($\theta < 45^\circ$).
 223 The strong southerly and southwesterly wind (black vectors in the top row) in the warm
 224 sector is associated with the southerly waves (black vectors in the bottom row), with an
 225 overall developing sea state ($\chi < 1.2$). The wind abruptly switches to northwesterly
 226 across the cold front. In response, strongly misaligned waves with $\theta > 100^\circ$ occur over
 227 a broad fetch west of the cold front, with χ rising above 1.2. As the front moves east-
 228 ward, a new area of misaligned waves is continuously generated in the far east, with the
 229 developing sea state ($\chi < 1.2$) progressively turning into a mixed sea state ($1.2 < \chi <$
 230 3) in the far west. Much of the sea state behind the cold front is a mixture of two wave
 231 categories: slightly older southerly wind waves forced by the warm sector southerly wind
 232 and newly generated younger short wind waves forced by the cold sector northwesterly
 233 wind (Figures 2 and 3).

234 These wind and wave evolutions from the model are consistent with the observa-
 235 tions at the Pioneer Array. Figure 3 shows the hourly time series of the near-surface me-
 236 teorological and wave measurements. During the pre-cold-front (gray-shaded period),
 237 southerly winds (black arrows) with >10 m/s and a developing sea state ($\chi \leq 1.2$) were
 238 observed. The waves were largely aligned with the wind (red arrows). After the cold front
 239 passage on December 6 at 12:00 UTC (red-shaded period), the near-surface air temper-
 240 ature and relative humidity dropped rapidly, and the wind direction switched to north-
 241 westerly, while the dominant wave direction continued to be southerly, indicating a large
 242 degree of wave-wind misalignment ($\theta \geq 100^\circ$) and a mixed sea state ($\chi > 1.2$). For
 243 this particular event, the wind waves remained misaligned with the winds for more than
 244 18 hours after the cold front, after which the waves gradually became aligned with the
 245 wind, and the wave age subsided below 1.2.

246 The adjacent NDBC buoys captured similar wave responses. The 2D wave spec-
 247 tra plots constructed from the 4 NDBC buoys (Figure 4) indicate that during the pre-
 248 cold-front, the dominant wave direction is southerly, with wave periods of 5-10s. Even
 249 after the cold front passes, these southerly surface waves persist, while new short waves
 250 with a period lower than 5s are generated from the northwest. While there is a reason-
 251 able range of regional variability across the buoys, the salient feature of the wave responses
 252 is broadly consistent across all the buoys examined. Compared to the Pioneer Array and

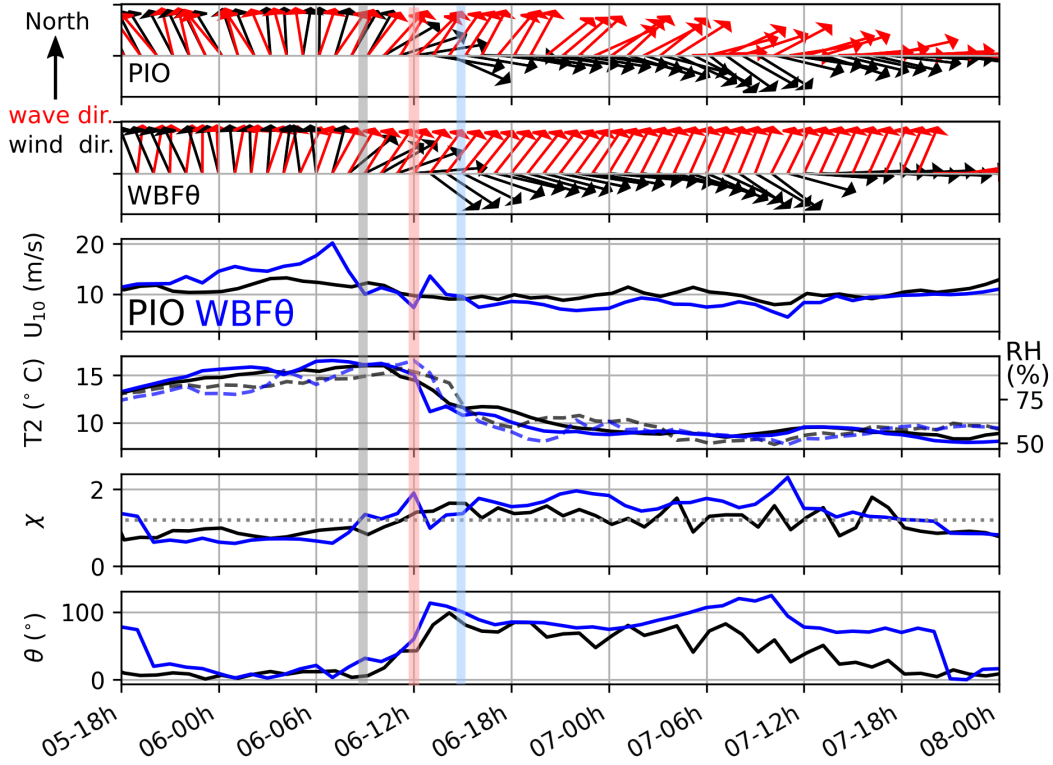


Figure 3. The top two panels show the observed and simulated (WBF θ) wind direction (black arrows) and wave peak direction (red arrows) around the passing of the atmospheric front on December 6, 2017. The length of the arrows in the top two panels is normalized. Gray, red, and blue shaded periods denote the pre-cold-front, cold-front, and post-cold-front shown in Figure 2. The following panels show the 10 m wind speed (U_{10} , m/s), air temperature (T2, solid line, °C), relative humidity (RH, dashed line, %), wave age, and misalignment angle (θ , °) from the Pioneer Array (black) and WBF θ (blue). The dotted gray line on the wave age panel denotes the wave age = 1.2.

253 the NDBC buoys, the simulation (WBF θ) also captures the characteristics of the atmo-
 254 spheric front and the observed wave evolution reasonably well. The model also captures
 255 the background easterly swell observed from the NDBC buoys.

256 Figure 5 shows the frequency-averaged wave energy density spectra (E_f) during
 257 the passage of the atmospheric front in WBF θ . The top row shows the average energy
 258 coming from the 90° sectors from the southwest to southeast direction, while the bot-
 259 tom row shows the energy coming from the 90° sectors from the west to north direction.
 260 Strong southerly wave energy builds under the warm sector ahead of the cold front and

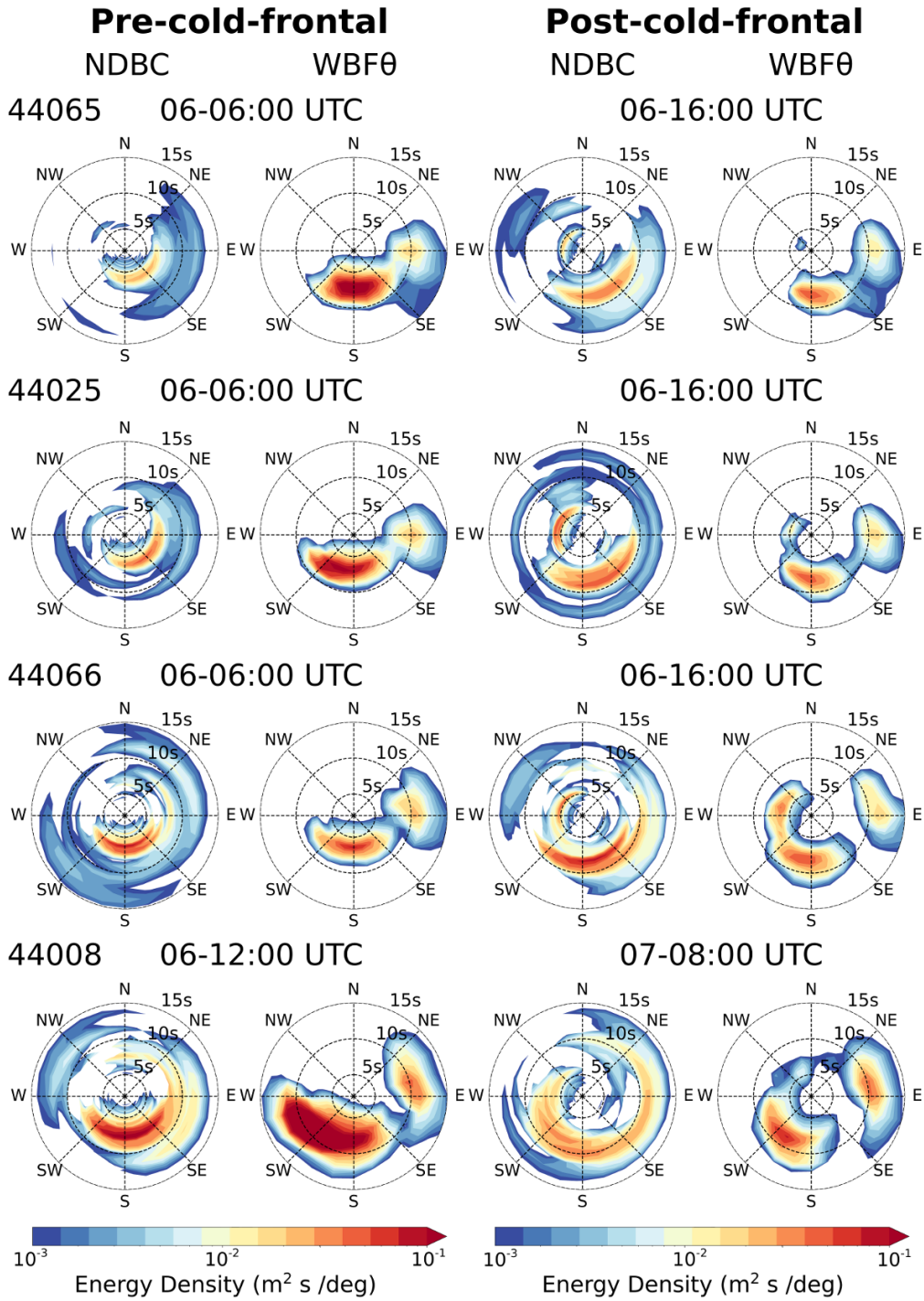


Figure 4. The 2D wave energy density spectra ($m^2 s / \text{deg}$) shown in the period space calculated from the 4 NDBC mooring locations, 44065, 44025, 44066, and 44008 (see Figure 2 for mooring locations) and the WBFθ run during a pre-cold-front (left column) and post-cold-front (right column) time.

261 dissipates as the cold front passes over the region. Meanwhile, the northwesterly winds
 262 behind the cold front generate new waves coming from the northwest, so the wave en-
 263 ergy from that direction grows following the cold front, creating mixed sea conditions.
 264 Note that the color scale on Figure 5 is different on both rows and indicates that the southerly
 265 energy is much stronger and dominant even after the cold front, leading to the observed
 266 wind and wave misalignment. As suggested in Figure 3, more than 18 hours after the
 267 passage of the cold front is needed for the waves to be aligned again and for the southerly
 268 wave energy under the warm sector to dissipate eventually.

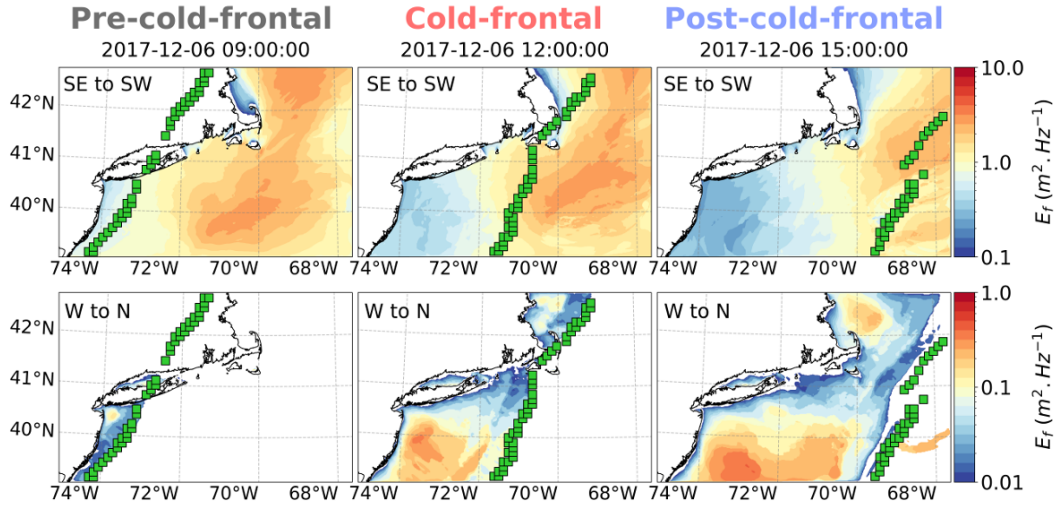


Figure 5. The frequency-averaged wave energy density spectra ($E_f, m^2.Hz^{-1}$) as simulated from the WBF θ run at 09:00 (pre-cold-front), 12:00 (cold-front) and 15:00 (post-cold-front) UTC on December 6, 2017. The green markers indicate the detected cold front using the Parfitt et al. (2017) algorithm. The top row shows the energy coming from the 90° sector from the southeast to southwest direction (SE to SW), while the bottom row shows the energy coming from the 90° sector from the west to north direction (W to N).

269 3.2 Impacts on surface drag and momentum flux

270 The WBF θ run is compared with the WBF run to reveal the effect of misaligned
 271 waves. For this, we will focus on differences in directly impacted variables: z_0 , C_D , τ ,
 272 and wind speeds at two different heights, 10 m (within the surface layer, U_{10}) and 110
 273 m (above the surface layer, U_{110}). We will also discuss the changes in turbulent heat flux

274 after that. For simplicity, we will compare the difference only at the post-cold-front (De-
 275 cember 6, 15:00 UTC).

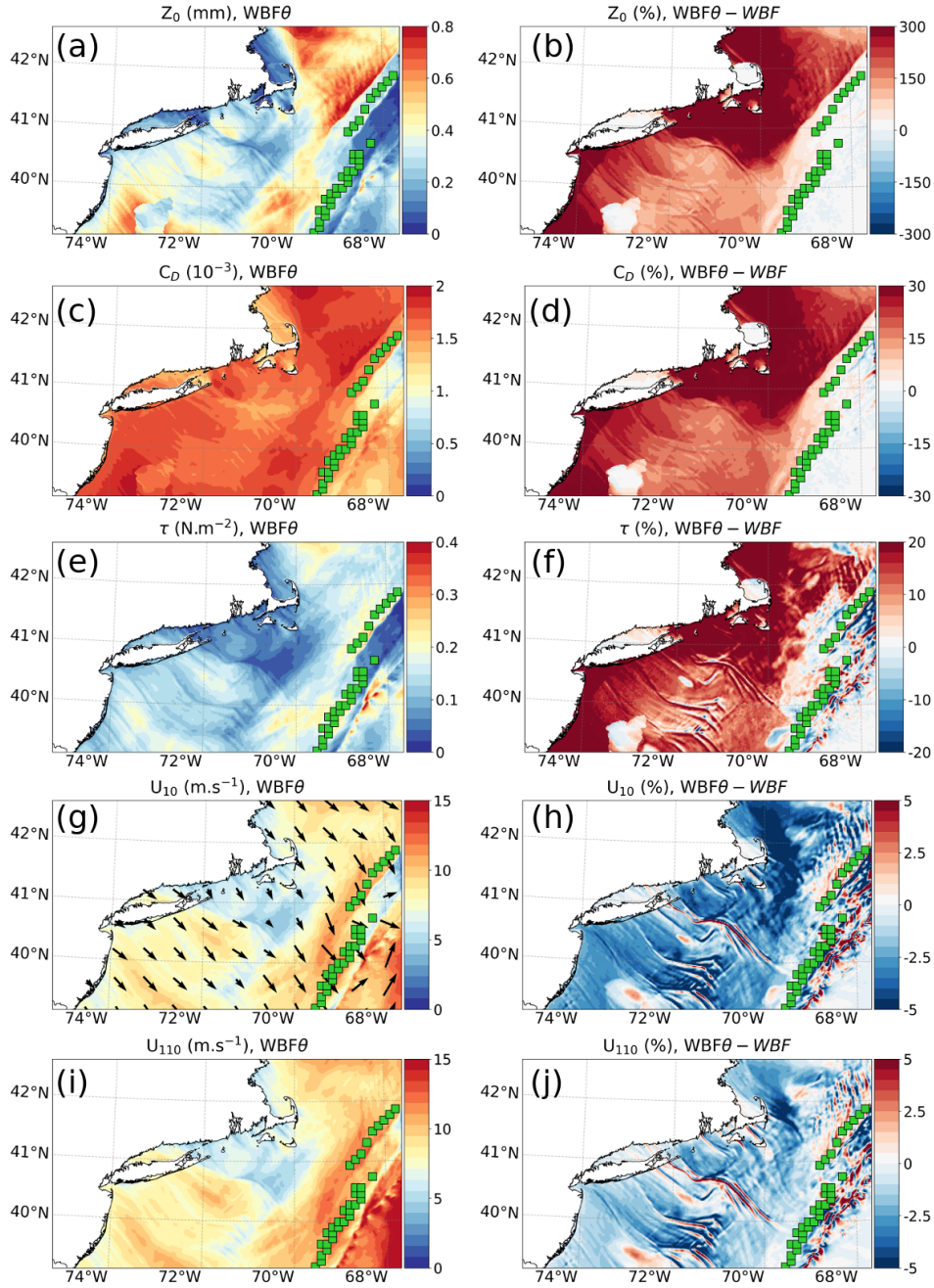


Figure 6. (a,c,e,g,i) shows the roughness length (z_0), drag coefficient (C_D), momentum flux (τ), surface wind speed (U_{10}) and wind speed at 110 m (U_{110}) from WBFθ and (b,d,f,h,j) the percent difference between WBFθ and WBF (%) after the passage of the cold front, at 15:00 UTC on December 6, 2017. The arrows overlaid on U_{10} indicate the direction of the surface wind. The green markers indicate the detected cold front using the Parfitt et al. (2017) algorithm.

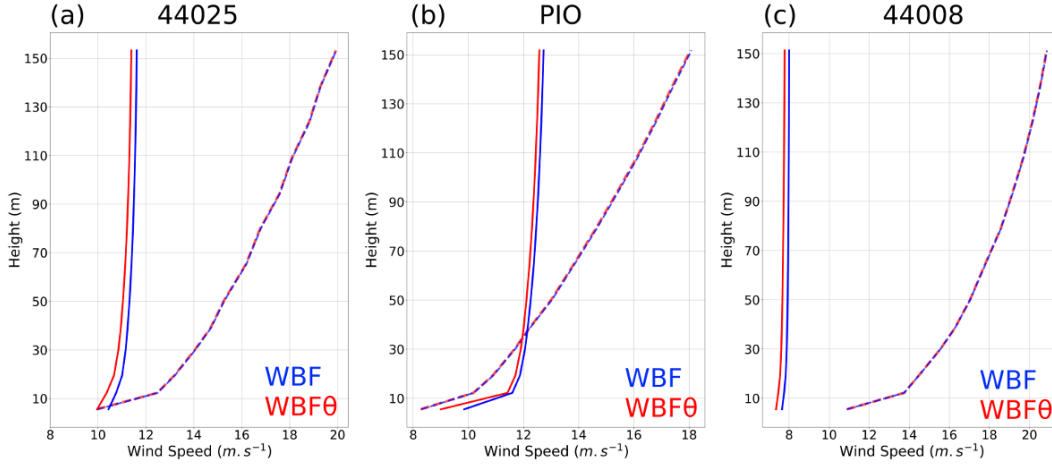


Figure 7. Vertical wind speed profiles from WBF (blue) and WBF θ (red) at (b) Pioneer Array location and (a,c) two NDBC moorings, 44025 and 44008. On each plot, a profile before (dashed) and a profile after (solid) the passage of the cold front is shown. For NDBC moorings (a,c), the times are chosen to be the same as in Figure 4, while for Pioneer Array (b), the times are chosen to be the pre-cold-front and post-cold-front shown in Figure 2.

276 The left column of Figure 6 shows WBF θ , and the right column shows the differ-
 277 ence between WBF θ and WBF, expressed as the percentage difference ($(\text{WBF}\theta - \text{WBF})$
 278 $/ \text{WBF}) \times 100$). East of the cold front, where the wave and wind are largely aligned, lit-
 279 tle difference is found in each of these four quantities. However, sizable increases are found
 280 in z_0 , C_D , and τ west of the cold front. The increase can be as high as 300% for z_0 , 30%
 281 for C_D , and 20% for τ , respectively. If area-averaged over the broad region west of the
 282 cold front, the increases are 185.7%, 19.3%, and 11%, respectively (Fig. 6a-d). Moreover,
 283 because of the increase in the surface drag, U_{10} is reduced in WBF θ by up to 5% (or 2%
 284 when area-averaged, Fig. 6g,h). The increased drag by the misaligned wave is also felt
 285 above the surface layer. Here, the wind at 110 m is chosen to show the impact above the
 286 surface layer (Figure 6i,j). U_{110} is reduced behind the cold front, having a coherent spa-
 287 tial pattern to that of U_{10} . However, the magnitude of the reduction above the surface
 288 layer is generally small (1-5% or 0.1-0.5 m.s^{-1} , Figure 6i,j). Figure 7 shows wind speed
 289 profiles at different NDBC moorings and Pioneer Array locations, confirming that the
 290 effect of increased drag by the misaligned waves on wind speed is largest in the surface
 291 layer and smaller above it.

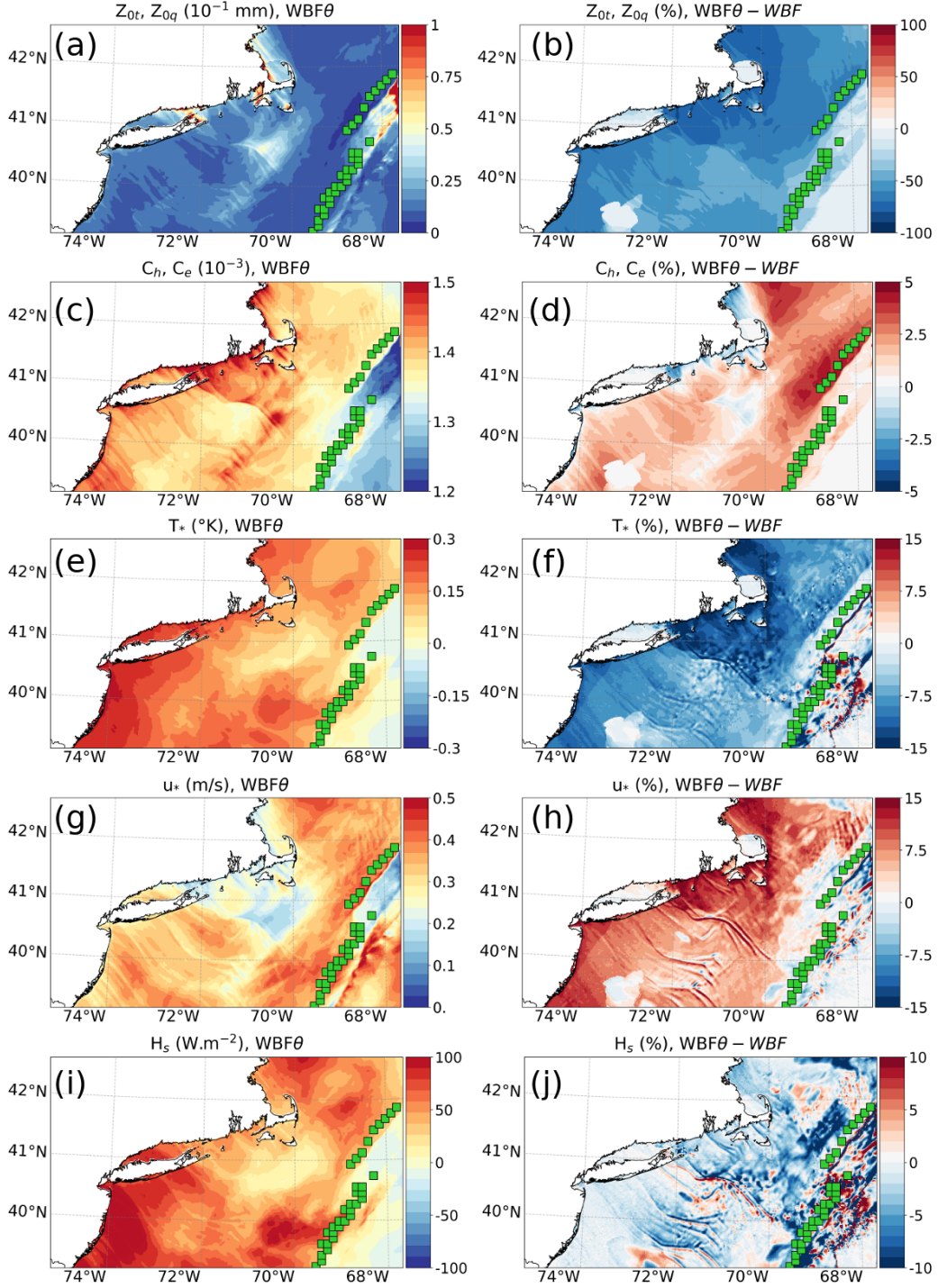


Figure 8. As in Figure 6, but for the scalar roughness length ($z_{0t}, z_{0q}, 10^{-1}mm$), the exchange coefficient for heat and moisture ($C_h, C_e, 10^{-3}$), the temperature scaling parameter (T_* , °K), the friction velocity (u_* , $m.s^{-1}$) and the sensible heat flux ($H_s, W.m^{-2}$). Heat flux is defined as positive upward.

292

3.3 Impacts on turbulent heat flux

293

294

295

296

297

298

299

300

301

302

303

304

305

The increases in surface roughness length due to misaligned waves also modify the upward sensible heat flux (H_s) and latent heat flux (H_l), reducing them west of the cold front by up to 10% (2.5% when area-averaged, Figure 8i,j and Figure 9c,d). This decrease in upward turbulent heat fluxes occurs despite a moderate increase in the exchange coefficients for heat and moisture (respectively C_h and C_e ; note that these are equal in the COARE3.5 algorithm) by up to 5% (Figure 8c,d). To investigate in more detail the impact on heat fluxes, based on WRF outputs from WBF and WBF θ and using COARE3.5 offline, we re-calculated the scalar roughness length for temperature and humidity (z_{0t} and z_{0q}), the surface exchange coefficients (C_h and C_e) and the specific humidity scaling parameter (q_*) which are not directly given by WRF outputs. Comparing the implementation of COARE3.5 in the MYNN surface scheme (Olson et al., 2021) to the COARE3.5 offline version, we are confident that the result would be the same if taken directly from WRF. z_{0t} is defined using the roughness Reynolds number (R_r) as:

$$R_r = \frac{u_* z_0}{\nu}, \quad (7)$$

$$z_{0t} = \frac{5.8e^{-5}}{R_r^{0.72}}, \quad (8)$$

306

307

308

where ν is the kinematic viscosity of the air. In COARE3.5, the moisture roughness length z_{0q} is equal to z_{0t} . The sensible and latent heat transfer coefficients are defined as

$$C_h(z, z_0, z_{0t}, \psi_m, \psi_h) = \left[\frac{\kappa}{\ln(z/z_0) - \psi_m(\zeta)} \right] \left[\frac{\kappa}{\ln(z/z_{0t}) - \psi_h(\zeta)} \right], \quad (9)$$

$$C_e(z, z_0, z_{0q}, \psi_m, \psi_h) = \left[\frac{\kappa}{\ln(z/z_0) - \psi_m(\zeta)} \right] \left[\frac{\kappa}{\ln(z/z_{0q}) - \psi_h(\zeta)} \right], \quad (10)$$

309

310

where $\psi_h(\zeta)$ is another empirical function of atmospheric stability. Because $z_{0q} = z_{0t}$ in COARE3.5, $C_e = C_h$.

311

312

313

314

The scalar roughness length z_{0t} is inversely proportional to the velocity roughness length z_0 , so an increase in z_0 due to wave misalignment (Fig. 6a,b) drives a decrease in z_{0t} (60% when area-averaged, Figure 8a,b). This increased resistance to turbulent scalar transport decreases the magnitude of the turbulent flux scale for temperature, T_* , by up

315 to 15%, Figure 8e,f. Note that T_* and the turbulent moisture flux scale q_* are defined
 316 to be negative for heat fluxes out of the ocean, so we plot $-T_*$ and $-q_*$ so that positive
 317 values of these quantities correspond to positive values of H_s and H_l . Overall, in Eq. 2,
 318 the increase in u_* due to misalignment (Figure 8g,h) is more than offset by the decrease
 319 in $-T_*$, resulting in a small decrease in sensible heat flux. Similarly, the decrease in z_{0q}
 320 induces a decrease in $-q_*$, which compensates for the increase in u_* and results in a small
 321 decrease in H_l overall, Equation 3 and Figure 9.

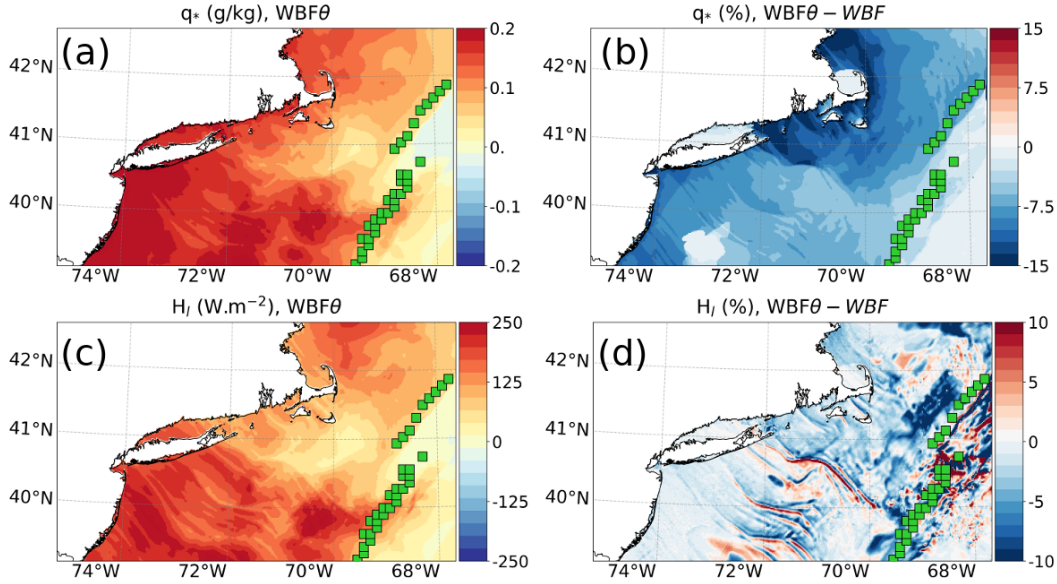


Figure 9. As in Figure 6 but for (a,b) the specific humidity scaling parameter (q_* , g/kg) and (c,d) the latent heat flux (H_l , $W.m^{-2}$).

322 4 Long-term characterization

323 Multi-year measurements of near-surface meteorology, surface waves, and direct co-
 324 variance fluxes from the Pioneer Array are used to examine the long-term characteris-
 325 tics of the misaligned waves under cold fronts. To do that, we first have to detect the
 326 cold front from the buoys. Because surface-based observations are used, the detected fronts
 327 can be deemed surface cold fronts. Here, we use the meridional surface wind (U_{10y}) and
 328 the 2-m air temperature (T_2). The cold front is identified when U_{10y} is shifted from southerly
 329 to northerly, with an additional criterion that the northerly (southerly) U_{10y} must per-
 330 sist over 2 hrs after (before) the frontal passage. We then check for a decrease in T_2 by
 331 $>3^\circ\text{C}$ between $t=-2$ hrs and $t=+8$ hrs. To ensure a strong shift in wind direction at the

332 passage of the cold front, we also require a change in wind direction of at least 60° . If
 333 all these conditions are met, the event is considered an atmospheric cold front over the
 334 Pioneer Array at $t=0$. Using this set of criteria, 86 atmospheric cold fronts were iden-
 335 tified from the 8-year Pioneer Array dataset. 55 of these events have co-located measure-
 336 ments of surface waves, which are used for subsequent analysis. Hereafter, we defined
 337 misaligned waves when the angle between wind and waves exceeds at least 60° . The re-
 338 sults presented here do not change appreciably with reasonable variations of criteria.

339 Figure 10a shows the histogram of the so-detected cold front occurrence as a func-
 340 tion of calendar months. Consistent with the previous studies (Parfitt et al., 2017; Reeder
 341 et al., 2021), the cold fronts are most frequently observed during the extended winter
 342 period (November - March), with 62 out of 86 events. Figure 10b shows the composite
 343 evolutions of θ across the fronts, indicating strongly misaligned waves at the cold front
 344 passage ($t=0$).

345 These fronts feature southerly wind (Figure 10c) with moderate speed (8 m/s, Fig-
 346 ure 10d) in the warm sector accompanied by a strong shift in wind direction from the
 347 warm to cold sectors exceeding at least 60° (Figure 10c). Because of moderate wind con-
 348 ditions in the warm sector, the sea state is generally characterized by a mixed sea ($1.2 <$
 349 $\chi < 2$), where wind-waves and some pre-existing swell co-exist, the condition that was
 350 also observed from the NDBC buoys (Figure 4). As the cold front passes and the winds
 351 change direction, the waves begin to be misaligned 1~2 hrs before the front, and once
 352 generated, the waves remain misaligned for 8 hours on average (Figure 10b).

353 We use the DCFS momentum flux measurements at the Pioneer Array to evalu-
 354 ate the accuracy of the parameterized momentum flux. Because DCFS data are avail-
 355 able for a shorter period (see Section 2.1), only 36 atmospheric front events were iden-
 356 tified from this period, of which 20 have led to misaligned waves ($\theta > 60^\circ$). Figure 11a,b
 357 shows the composite evolutions of the directly measured C_d and τ (black) for the fronts
 358 that generated the misaligned waves. With the state variables measured from the Pi-
 359 oneer Array, we then calculated C_d and τ without misaligned waves (blue, Eq. 5) and
 360 with misaligned waves (red, Eq. 6). The result shows that the estimated momentum flux
 361 with misaligned waves is higher than without by 16.5% at $t=0$ and 6.6% for 8 hours af-
 362 ter the cold front. When averaged over the 8 hours after the cold front, this elevated wind
 363 stress with misaligned waves is closer to the DCFS estimates (bias is reduced from 4.9%

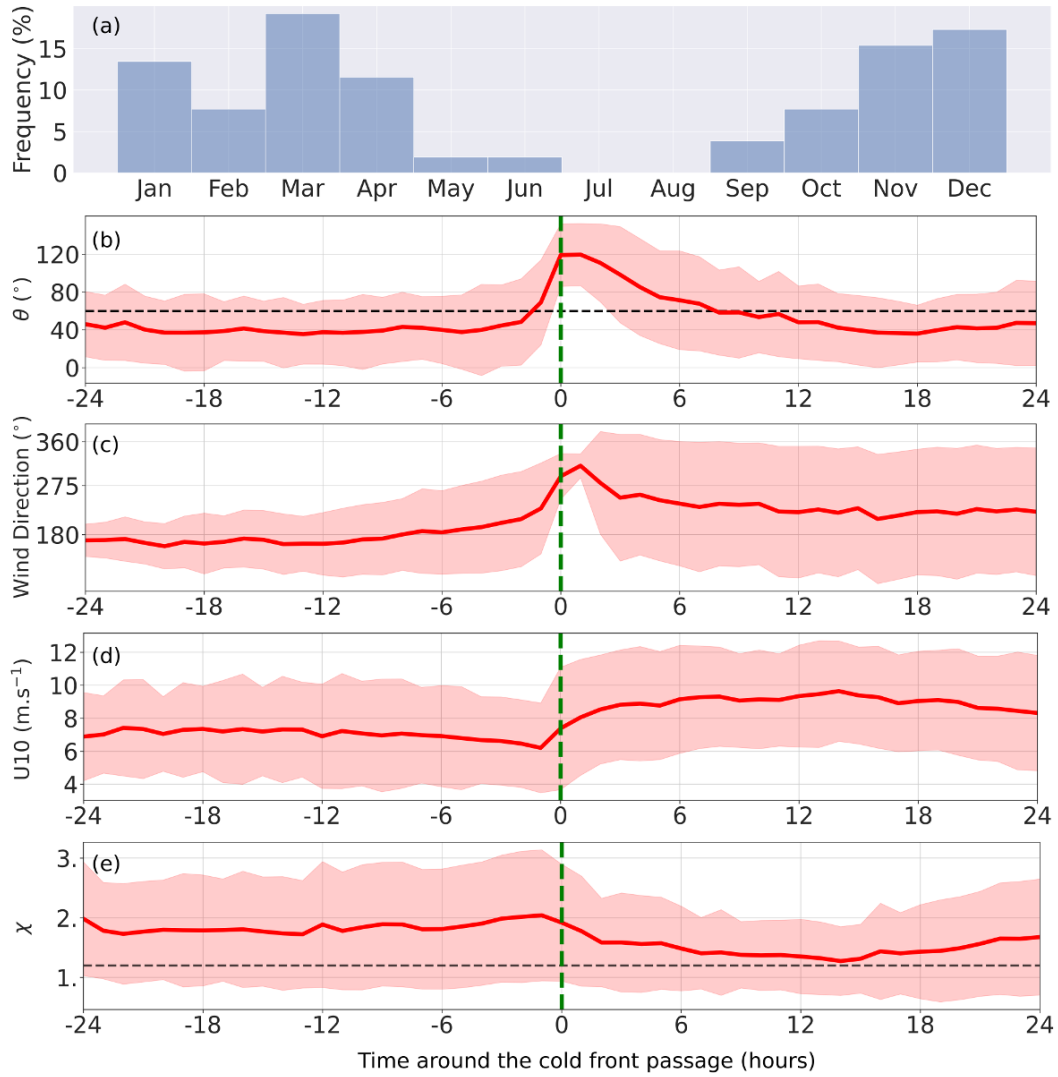


Figure 10. (a) Probability of occurrence of cold front per month (%) calculated using the Pioneer Array data from December 2014 to November 2022. (b,c,d,e) Composite evolutions of (b) misalignment angle (θ , $^\circ$), (c) wind direction ($^\circ$, 0 means northerly), (d) wind speed (m/s), and (e) wave age for the detected atmospheric cold fronts. The shaded envelopes represent ± 1 standard deviations. In (b), the dashed line indicates the 60° line; in (e), a wave age 1.2. The vertical green line indicates the cold front at a $t=0$.

364 to 1.1% for τ and from 6% to 1.1% for C_d). The results also corroborate the modeling
 365 results (WBF vs. WBF θ).

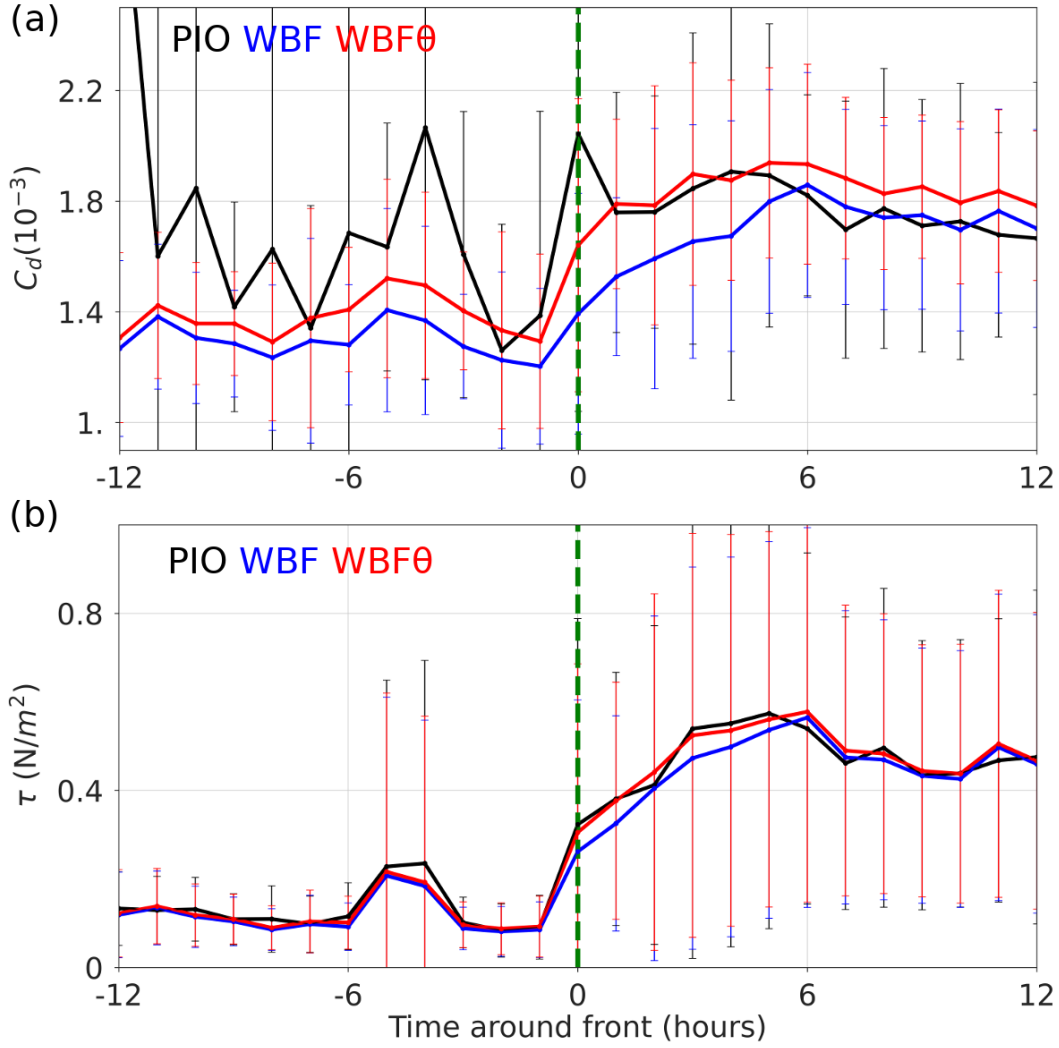


Figure 11. Composite evolution of the parameterized (a) drag coefficient ($C_d, 10^{-3}$) and (b) momentum flux (τ, Nm^{-2}) calculated offline using the COARE3.5 (WBF θ , red) with and (WBF, blue) without the misaligned wave effect, in comparison to direct covariance flux measurements from the Pioneer Array (PIO, black). The error bars represent ± 1 standard deviation. The vertical green line indicates the cold front at $t=0$.

366 **5 Conclusion and Discussions**

367 Using the multi-year in-situ observations and numerical model simulations, this study
 368 examined the nature and impacts of the misaligned surface waves behind the passing of
 369 atmospheric cold fronts off the coast of New England. A case study investigation indi-
 370 cates that an atmospheric cold front generates a significant fetch of misaligned waves be-
 371 hind it, comparable to the lateral extent of the extratropical cyclones in which the front

372 is embedded. Over a vast region of misaligned waves propagating with the front, the model
373 simulations indicate that misaligned waves significantly increase the roughness length,
374 drag and enthalpy exchange coefficients, and wind stress. In response to increased sur-
375 face drag, the near-surface wind speed is reduced, reducing upward turbulent heat fluxes.
376 Note that the decrease in upward turbulent heat flux is despite the moderate increase
377 in surface heat and moisture exchange coefficients. Indeed, the scalar roughness decreased
378 as the velocity roughness increased, decreasing the temperature and humidity scaling pa-
379 rameters and increasing the friction velocity. This leads to compensating effects on both
380 latent and sensible heat fluxes. Hence, the magnitudes of the responses in turbulent heat
381 fluxes are modest.

382 The long-term analysis using the Pioneer Array data allowed us to detect over 50
383 atmospheric cold fronts, which generated misaligned waves behind them. Once gener-
384 ated, these waves remain misaligned with the wind for 8 hours on average. This percent-
385 age of atmospheric cold front detection, of course, depends on the chosen threshold, but
386 the results are qualitatively similar.

387 The current COARE wave-based bulk flux parameterization assumes that waves
388 and wind are aligned (Eq. 5). A simple modification to this formulation is suggested to
389 represent the misaligned wave effect as in Eq. (6), which produces overall improved es-
390 timates of the parameterized momentum flux under this condition. As discussed exten-
391 sively in Sauvage et al. (2023), equivalent to incorporating the directional misalignment
392 in COARE is simply replacing the peak wave period with the mean wave period to cal-
393 culate the wave age in Eq. (5) (See their Eq. 12). The rationale is that the spectrally-
394 averaged wave period more accurately depicts a sea state that is a mixture of wind waves
395 of ranging frequencies, as in Figure 4.

396 Finally, the impacts of the improved surface stress on the wind profile appear lim-
397 ited to the surface layer. An important caveat to consider is that the present analysis
398 mainly concerns the “instantaneous” impacts of the altered momentum flux, whereas,
399 in the nature and long-term coupled runs, the mixed layer depth will likely respond to
400 different turbulent momentum and heat fluxes, thereby greatly affecting state variables
401 such as sea surface temperature. These effects cannot be captured in the short 3-day sim-
402 ulations. Longer simulations that fully resolve the interactions between the atmospheric
403 fronts and surface waves are needed to determine the impacts on kinematic and ther-

404 modynamic properties in the PBL and upper ocean and possibly the evolution of the at-
405 mospheric fronts.

406 **6 Open Research**

407 ERA5 data are made available by Copernicus Climate Change Service ([https://](https://cds.climate.copernicus.eu)
408 cds.climate.copernicus.eu), Mercator by Copernicus Marine Environment Monitor-
409 ing Service (<https://doi.org/10.48670/moi-00016>), and global 3-hourly spectral wave
410 analyses by Ifremer (<ftp://ftp.ifremer.fr/ifremer/ww3/HINDCAST/GLOBAL>). OOI Pi-
411 oneer Array data are obtained from <https://dataexplorer.oceanobservatories.org>,
412 and NDBC data from <https://www.ndbc.noaa.gov/>. WW3 is distributed via [https://](https://github.com/NOAA-EMC/WW3)
413 github.com/NOAA-EMC/WW3, WRF <https://github.com/wrf-model/WRF>, and ROMS [https://](https://www.myroms.org/)
414 www.myroms.org/. The SCOAR codes are available via [https://github.com/SCOAR-model/](https://github.com/SCOAR-model/SCOAR)
415 [SCOAR](https://github.com/SCOAR-model/SCOAR). The modified COARE3.5 code is available at [https://github.com/cesarsauvage/](https://github.com/cesarsauvage/COARE3.5_modified_Sauvage-et-al.-2023)
416 [COARE3.5_modified_Sauvage-et-al.-2023](https://github.com/cesarsauvage/COARE3.5_modified_Sauvage-et-al.-2023) and the model outputs at Zenodo.

417 **Acknowledgments**

418 This research was supported by NOAA (NA19OAR4310376), NASA (80NSSC21K1524),
419 NSF (OCE-2148120), and DOE (DE-EE0009424). Additionally, HS acknowledges NSF
420 (OCE-2022846). The WHOI High-Performance Computing Facility provided the com-
421 puting resources.

References

- 422
- 423 Arduin, F., O'Reilly, W. C., Herbers, T. H. C., & Jessen, P. F. (2003). Swell
424 Transformation across the Continental Shelf. Part I: Attenuation and Direc-
425 tional Broadening. *Journal of Physical Oceanography*, *33*(9), 1921–1939. doi:
426 10.1175/1520-0485(2003)033<1921:STATCS>2.0.CO;2
- 427 Arduin, F., & Roland, A. (2012). Coastal wave reflection, directional spread,
428 and seismoacoustic noise sources. *Journal of Geophysical Research: Oceans*,
429 *117*(C11). doi: 10.1029/2011JC007832
- 430 Babanin, A. (2011). *Breaking and Dissipation of Ocean Surface Waves*. Cambridge:
431 Cambridge University Press. doi: 10.1017/CBO9780511736162
- 432 Battjes, J. A., & Janssen, J. P. F. M. (1978). Energy Loss and Set-Up Due
433 to Breaking of Random Waves. *Coastal Engineering*, 569–587. doi:
434 10.1061/9780872621909.034
- 435 Berry, G., Reeder, M. J., & Jakob, C. (2011). A global climatology of atmospheric
436 fronts. *Geophysical Research Letters*, *38*(4). doi: 10.1029/2010GL046451
- 437 Bjerknes, J., & Solberg, H. (1922). Life of the Cyclones and the Polar Front Theory
438 of Atmospheric Circulation. *Geophysisks Publikationer*, *3*(1), 18.
- 439 Cao, Y., Li, C., & Dong, C. (2020). Atmospheric Cold Front-Generated Waves in
440 the Coastal Louisiana. *Journal of Marine Science and Engineering*, *8*(11), 900.
441 doi: 10.3390/jmse8110900
- 442 Catto, J. L., & Pfahl, S. (2013). The importance of fronts for extreme precipita-
443 tion. *Journal of Geophysical Research: Atmospheres*, *118*(19), 10,791–10,801.
444 doi: 10.1002/jgrd.50852
- 445 Chen, F., & Dudhia, J. (2001). Coupling an Advanced Land Surface–Hydrology
446 Model with the Penn State–NCAR MM5 Modeling System. Part I: Model Im-
447 plementation and Sensitivity. *Monthly Weather Review*, *129*(4), 569–585. doi:
448 10.1175/1520-0493(2001)129<0569:CAALSH>2.0.CO;2
- 449 Chen, G., Chapron, B., Ezraty, R., & Vandemark, D. (2002). A Global View of
450 Swell and Wind Sea Climate in the Ocean by Satellite Altimeter and Scat-
451 terometer. *Journal of Atmospheric and Oceanic Technology*, *19*(11), 1849–
452 1859. doi: 10.1175/1520-0426(2002)019<1849:AGVOSA>2.0.CO;2
- 453 Chen, S. S., & Curcic, M. (2016). Ocean surface waves in Hurricane Ike (2008) and
454 Superstorm Sandy (2012): Coupled model predictions and observations. *Ocean*

- 455 *Modelling*, 103, 161–176. doi: 10.1016/j.ocemod.2015.08.005
- 456 Chen, S. S., Zhao, W., Donelan, M. A., & Tolman, H. L. (2013). Directional
457 Wind–Wave Coupling in Fully Coupled Atmosphere–Wave–Ocean Models:
458 Results from CBLAST-Hurricane. *Journal of the Atmospheric Sciences*,
459 70(10), 3198–3215. doi: 10.1175/JAS-D-12-0157.1
- 460 Chen, X., Ginis, I., & Hara, T. (2020). Impact of Shoaling Ocean Surface Waves
461 on Wind Stress and Drag Coefficient in Coastal Waters: 2. Tropical Cy-
462 clones. *Journal of Geophysical Research: Oceans*, 125(7), e2020JC016223.
463 doi: 10.1029/2020JC016223
- 464 Edson, J. B., Jampana, V., Weller, R. A., Bigorre, S. P., Plueddemann, A. J.,
465 Fairall, C. W., ... Hersbach, H. (2013). On the Exchange of Momentum
466 over the Open Ocean. *Journal of Physical Oceanography*, 43(8), 1589–1610.
467 doi: 10.1175/JPO-D-12-0173.1
- 468 Egbert, G. D., & Erofeeva, S. Y. (2002). Efficient Inverse Modeling of Barotropic
469 Ocean Tides. *Journal of Atmospheric and Oceanic Technology*, 19(2), 183–204.
470 doi: 10.1175/1520-0426(2002)019<0183:EIMOBO>2.0.CO;2
- 471 Fairall, C. W., Bradley, E. F., Hare, J. E., Grachev, A. A., & Edson, J. B.
472 (2003). Bulk Parameterization of Air–Sea Fluxes: Updates and Verifica-
473 tion for the COARE Algorithm. *Journal of Climate*, 16(4), 571–591. doi:
474 10.1175/1520-0442(2003)016<0571:BPOASF>2.0.CO;2
- 475 Fairall, C. W., Bradley, E. F., Rogers, D. P., Edson, J. B., & Young, G. S. (1996).
476 Bulk parameterization of air-sea fluxes for Tropical Ocean–Global Atmosphere
477 Coupled–Ocean Atmosphere Response Experiment. *Journal of Geophysical
478 Research: Oceans*, 101(C2), 3747–3764. doi: 10.1029/95JC03205
- 479 Grachev, A. A., & Fairall, C. W. (2001). Upward Momentum Transfer in the Marine
480 Boundary Layer. *Journal of Physical Oceanography*, 31(7), 1698–1711. doi: 10
481 .1175/1520-0485(2001)031<1698:UMTITM>2.0.CO;2
- 482 Guo, B., Subrahmanyam, M. V., & Li, C. (2020). Waves on Louisiana Continental
483 Shelf Influenced by Atmospheric Fronts. *Scientific Reports*, 10(1), 272. doi: 10
484 .1038/s41598-019-55578-w
- 485 Haidvogel, D. B., Arango, H. G., Hedstrom, K., Beckmann, A., Malanotte-
486 Rizzoli, P., & Shechetkin, A. F. (2000). Model evaluation experiments
487 in the North Atlantic Basin: Simulations in nonlinear terrain-following co-

- 488 ordinates. *Dynamics of Atmospheres and Oceans*, 32(3), 239–281. doi:
489 10.1016/S0377-0265(00)00049-X
- 490 Hanley, K. E., & Belcher, S. E. (2008). Wave-Driven Wind Jets in the Marine At-
491 mospheric Boundary Layer. *Journal of the Atmospheric Sciences*, 65(8), 2646–
492 2660. doi: 10.1175/2007JAS2562.1
- 493 Hanley, K. E., Belcher, S. E., & Sullivan, P. P. (2010). A Global Climatology of
494 Wind-Wave Interaction. *Journal of Physical Oceanography*, 40(6), 1263–1282.
495 doi: 10.1175/2010JPO4377.1
- 496 Hasselmann, S., Hasselmann, K., Allender, J. H., & Barnett, T. P. (1985). Compu-
497 tations and Parameterizations of the Nonlinear Energy Transfer in a Gravity-
498 Wave Spectrum. Part II: Parameterizations of the Nonlinear Energy Transfer
499 for Application in Wave Models. *Journal of Physical Oceanography*, 15(11),
500 1378–1391. doi: 10.1175/1520-0485(1985)015<1378:CAPOTN>2.0.CO;2
- 501 Hersbach, H., Bell, B., Berrisford, P., Hirahara, S., Horányi, A., Muñoz-Sabater, J.,
502 ... Thépaut, J.-N. (2020). The ERA5 global reanalysis. *Quarterly Journal of*
503 *the Royal Meteorological Society*, 146(730), 1999–2049. doi: 10.1002/qj.3803
- 504 Hewson, T. D. (1998). Objective fronts. *Meteorological Applications*, 5(1), 37–65.
505 doi: 10.1017/S1350482798000553
- 506 Hong, S.-Y., & Lim, J.-O. J. (2006). The WRF Single-Moment 6-Class Microphysics
507 Scheme (WSM6). *JOURNAL OF THE KOREAN METEOROLOGICAL SO-*
508 *CIETY*.
- 509 Hsu, J.-Y., Lien, R.-C., D’Asaro, E. A., & Sanford, T. B. (2019). Scaling of Drag
510 Coefficients Under Five Tropical Cyclones. *Geophysical Research Letters*,
511 46(6), 3349–3358. doi: 10.1029/2018GL081574
- 512 Iacono, M. J., Delamere, J. S., Mlawer, E. J., Shephard, M. W., Clough, S. A., &
513 Collins, W. D. (2008). Radiative forcing by long-lived greenhouse gases: Cal-
514 culations with the AER radiative transfer models. *Journal of Geophysical*
515 *Research: Atmospheres*, 113(D13). doi: 10.1029/2008JD009944
- 516 Jiménez, P. A., Dudhia, J., González-Rouco, J. F., Navarro, J., Montávez, J. P.,
517 & García-Bustamante, E. (2012). A Revised Scheme for the WRF Sur-
518 face Layer Formulation. *Monthly Weather Review*, 140(3), 898–918. doi:
519 10.1175/MWR-D-11-00056.1
- 520 Kim, J.-Y., Kaihatu, J., Chang, K.-A., Sun, S.-H., Huff, T. P., & Feagin, R. A.

- 521 (2020). Effect of Cold Front-Induced Waves Along Wetlands Boundaries.
 522 *Journal of Geophysical Research: Oceans*, *125*(12), e2020JC016603. doi:
 523 10.1029/2020JC016603
- 524 Kukulka, T., & Hara, T. (2005). Momentum flux budget analysis of wind-driven air-
 525 water interfaces. *Journal of Geophysical Research: Oceans*, *110*(C12). doi: 10
 526 .1029/2004JC002844
- 527 Large, W. G., McWilliams, J. C., & Doney, S. C. (1994). Oceanic vertical mixing: A
 528 review and a model with a nonlocal boundary layer parameterization. *Reviews*
 529 *of Geophysics*, *32*(4), 363–403. doi: 10.1029/94RG01872
- 530 Lellouche, J.-M., Greiner, E., Le Galloudec, O., Garric, G., Regnier, C., Drevillon,
 531 M., ... Le Traon, P.-Y. (2018). Recent updates to the Copernicus Marine
 532 Service global ocean monitoring and forecasting real-time 1/12° high-resolution
 533 system. *Ocean Science*, *14*(5), 1093–1126. doi: 10.5194/os-14-1093-2018
- 534 Liu, Q., Rogers, W. E., Babanin, A. V., Young, I. R., Romero, L., Zieger, S., ...
 535 Guan, C. (2019). Observation-Based Source Terms in the Third-Generation
 536 Wave Model WAVEWATCH III: Updates and Verification. *Journal of Physical*
 537 *Oceanography*, *49*(2), 489–517. doi: 10.1175/JPO-D-18-0137.1
- 538 Makin, V. K., Kudryavtsev, V. N., & Mastenbroek, C. (1995). Drag of the sea sur-
 539 face. *Boundary-Layer Meteorology*, *73*(1), 159–182. doi: 10.1007/BF00708935
- 540 Nakanishi, M., & Niino, H. (2009). Development of an Improved Turbulence Closure
 541 Model for the Atmospheric Boundary Layer. *Journal of the Meteorological So-*
 542 *ciety of Japan. Ser. II*, *87*(5), 895–912. doi: 10.2151/jmsj.87.895
- 543 Olson, J. B., Smirnova, T., Kenyon, J. S., Turner, D. D., Brown, J. M., Zheng, W.,
 544 & Green, B. W. (2021). A Description of the MYNN Surface-Layer Scheme.
 545 *NOAA Technical Memorandum OAR GSL*. doi: 10.25923/F6A8-BC75
- 546 Parfitt, R., Czaja, A., Minobe, S., & Kuwano-Yoshida, A. (2016). The atmospheric
 547 frontal response to SST perturbations in the Gulf Stream region. *Geophysical*
 548 *Research Letters*, *43*(5), 2299–2306. doi: 10.1002/2016GL067723
- 549 Parfitt, R., Czaja, A., & Seo, H. (2017). A simple diagnostic for the detection of
 550 atmospheric fronts. *Geophysical Research Letters*, *44*(9), 4351–4358. doi: 10
 551 .1002/2017GL073662
- 552 Phillips, O. M. (1966). *The Dynamics of the Upper Ocean*. Cambridge U.P.
- 553 Porchetta, S., Temel, O., Muñoz-Esparza, D., Reuder, J., Monbaliu, J., Van Beeck,

- 554 J., & Van Lipzig, N. (2019). A new roughness length parameterization ac-
 555 counting for wind–wave (mis)alignment. *Atmospheric Chemistry and Physics*,
 556 *19*(10), 6681–6700. doi: 10.5194/acp-19-6681-2019
- 557 Porchetta, S., Temel, O., Warner, J., Muñoz-Esparza, D., Monbaliu, J., Van Beeck,
 558 J., & Van Lipzig, N. (2021). Evaluation of a roughness length parametrization
 559 accounting for wind–wave alignment in a coupled atmosphere–wave model.
 560 *Quarterly Journal of the Royal Meteorological Society*, *147*(735), 825–846. doi:
 561 10.1002/qj.3948
- 562 Rasclé, N., & Ardhuin, F. (2013). A global wave parameter database for geophysical
 563 applications. Part 2: Model validation with improved source term parameteri-
 564 zation. *Ocean Modelling*, *70*, 174–188. doi: 10.1016/j.ocemod.2012.12.001
- 565 Reeder, M. J., Spengler, T., & Spensberger, C. (2021). The Effect of Sea Surface
 566 Temperature Fronts on Atmospheric Frontogenesis. *Journal of the Atmospheric*
 567 *Sciences*, *78*(6), 1753–1771. doi: 10.1175/JAS-D-20-0118.1
- 568 Reichl, B. G., Hara, T., & Ginis, I. (2014). Sea state dependence of the wind
 569 stress over the ocean under hurricane winds. *Journal of Geophysical Research:*
 570 *Oceans*, *119*(1), 30–51. doi: 10.1002/2013JC009289
- 571 Sauvage, C., Seo, H., Clayson, C. A., & Edson, J. B. (2023). Improving Wave-Based
 572 Air–Sea Momentum Flux Parameterization in Mixed Seas. *Journal of Geophys-*
 573 *ical Research: Oceans*, *128*(3), e2022JC019277. doi: 10.1029/2022JC019277
- 574 Seo, H., Miller, A. J., & Norris, J. R. (2016). Eddy–Wind Interaction in the Cali-
 575 fornia Current System: Dynamics and Impacts. *Journal of Physical Oceanogra-*
 576 *phy*, *46*(2), 439–459. doi: 10.1175/JPO-D-15-0086.1
- 577 Seo, H., Miller, A. J., & Roads, J. O. (2007). The Scripps Coupled
 578 Ocean–Atmosphere Regional (SCOAR) Model, with Applications in the
 579 Eastern Pacific Sector. *Journal of Climate*, *20*(3), 381–402. doi: 10.1175/
 580 JCLI4016.1
- 581 Seo, H., O’Neill, L. W., Bourassa, M. A., Czaja, A., Drushka, K., Edson, J. B., ...
 582 Wang, Q. (2023). Ocean Mesoscale and Frontal-Scale Ocean–Atmosphere
 583 Interactions and Influence on Large-Scale Climate: A Review. *Journal of*
 584 *Climate*, *36*(7), 1981–2013. doi: 10.1175/JCLI-D-21-0982.1
- 585 Seo, H., Song, H., O’Neill, L. W., Mazloff, M. R., & Cornuelle, B. D. (2021).
 586 Impacts of ocean currents on the South Indian Ocean extratropical storm

- 587 track through the relative wind effect. *Journal of Climate*, 1–61. doi:
588 10.1175/JCLI-D-21-0142.1
- 589 Seo, H., Subramanian, A. C., Miller, A. J., & Cavanaugh, N. R. (2014). Cou-
590 pled Impacts of the Diurnal Cycle of Sea Surface Temperature on the Mad-
591 den–Julian Oscillation. *Journal of Climate*, 27(22), 8422–8443. doi:
592 10.1175/JCLI-D-14-00141.1
- 593 Shchepetkin, A. F., & McWilliams, J. C. (2005). The regional oceanic model-
594 ing system (ROMS): A split-explicit, free-surface, topography-following-
595 coordinate oceanic model. *Ocean Modelling*, 9(4), 347–404. doi: 10.1016/
596 j.ocemod.2004.08.002
- 597 Shin, H. H., Hong, S.-Y., & Dudhia, J. (2012). Impacts of the Lowest Model Level
598 Height on the Performance of Planetary Boundary Layer Parameterizations.
599 *Monthly Weather Review*, 140(2), 664–682. doi: 10.1175/MWR-D-11-00027.1
- 600 Skamarock, C., Klemp, B., Dudhia, J., Gill, O., Liu, Z., Berner, J., . . . Huang, X.-y.
601 (2019). A Description of the Advanced Research WRF Model Version 4.1. (*No.*
602 *NCAR/TN-556+STR*). doi: 10.5065/1dfh-6p97
- 603 Soster, F., & Parfitt, R. (2022). On Objective Identification of Atmospheric Fronts
604 and Frontal Precipitation in Reanalysis Datasets. *Journal of Climate*, 35(14),
605 4513–4534. doi: 10.1175/JCLI-D-21-0596.1
- 606 Steffen, J., Seo, H., Clayson, C. A., Pei, S., & Shinoda, T. (2023). Impacts of tidal
607 mixing on diurnal and intraseasonal air-sea interactions in the Maritime Con-
608 tinent. *Deep Sea Research Part II: Topical Studies in Oceanography*, 212,
609 105343. doi: 10.1016/j.dsr2.2023.105343
- 610 Stopa, J. E., Ardhuin, F., Babanin, A., & Zieger, S. (2016). Comparison and valida-
611 tion of physical wave parameterizations in spectral wave models. *Ocean Mod-*
612 *elling*, 103, 2–17. doi: 10.1016/j.ocemod.2015.09.003
- 613 Sullivan, P. P., Edson, J. B., Hristov, T., & McWilliams, J. C. (2008). Large-Eddy
614 Simulations and Observations of Atmospheric Marine Boundary Layers above
615 Nonequilibrium Surface Waves. *Journal of the Atmospheric Sciences*, 65(4),
616 1225–1245. doi: 10.1175/2007JAS2427.1
- 617 The WAVEWATCH III Development Group, W. (2019). *User manual and system*
618 *documentation of WAVEWATCH III R© version 6.07* (Tech. Note 333). Col-
619 lege Park, MD, USA,: NOAA/NWS/NCEP/MMAB,.

- 620 Tolman, H. L., Balasubramanian, B., Burroughs, L. D., Chalikov, D. V., Chao,
621 Y. Y., Chen, H. S., & Gerald, V. M. (2002). Development and Implemen-
622 tation of Wind-Generated Ocean Surface Wave Models at NCEP. *Weather
623 and Forecasting*, *17*(2), 311–333. doi: 10.1175/1520-0434(2002)017<0311:
624 DAIOWG>2.0.CO;2
- 625 Trowbridge, J., Weller, R., Kelley, D., Dever, E., Plueddemann, A., Barth, J. A., &
626 Kawka, O. (2019). The Ocean Observatories Initiative. *Frontiers in Marine
627 Science*, *6*.
- 628 Zheng, Y., Alapaty, K., Herwehe, J. A., Genio, A. D. D., & Niyogi, D. (2016). Im-
629 proving High-Resolution Weather Forecasts Using the Weather Research and
630 Forecasting (WRF) Model with an Updated Kain–Fritsch Scheme. *Monthly
631 Weather Review*, *144*(3), 833–860. doi: 10.1175/MWR-D-15-0005.1
- 632 Zhou, X., Hara, T., Ginis, I., D’Asaro, E., Hsu, J.-Y., & Reichl, B. G. (2022). Drag
633 Coefficient and Its Sea State Dependence under Tropical Cyclones. *Journal of
634 Physical Oceanography*, *52*(7), 1447–1470. doi: 10.1175/JPO-D-21-0246.1